

FFV-PINN: A Fast Physics-Informed Neural Network with Simplified Finite Volume Discretization and Residual Correction

Chang Wei^a, Yuchen Fan^a, Jian Cheng Wong^b, Chin Chun Ooi^b, Heyang
Wang^{a,*}, Pao-Hsiung Chiu^{b,**}

^a*School of Mechanical Engineering, Tianjin University, Tianjin, 300350, China*

^b*Institute of High Performance Computing, Agency for Science, Technology and Research
(A*STAR), 138632, Singapore*

Abstract

With the growing application of deep learning techniques in computational physics, physics-informed neural networks (PINNs) have emerged as a major research focus. However, today's PINNs encounter several limitations. Firstly, during the construction of the loss function using automatic differentiation, PINNs often neglect information from neighboring points, which hinders their ability to enforce physical constraints and diminishes their accuracy. Furthermore, issues such as instability and poor convergence persist during PINN training, limiting their applicability to complex fluid dynamics problems. To address these challenges, this paper proposes a fast physics-informed neural network framework that integrates a simplified finite volume method (FVM) and residual correction loss term, referred to as Fast Finite Volume PINN (FFV-PINN). FFV-PINN utilizes a simplified FVM discretization for the convection term, which is one of the main sources of instability, with an accompanying improvement in the dispersion and dissipation behavior. Unlike traditional FVM, which requires careful selection of an appropriate discretization scheme based on the specific physics of the problem such as the sign of the convection term and relative magnitudes of

*Corresponding author at: School of Mechanical Engineering, Tianjin University, Tianjin, 300350, China. *E-mail address:* heyang.wang@tju.edu.cn (H. Wang).

**Corresponding author at: Institute of High Performance Computing, Agency for Science, Technology and Research (A*STAR), 138632, Singapore. *E-mail address:* chiuph@star.edu.sg (P-H. Chiu).

convection and diffusion, the FFV-PINN outputs can be simply and directly harnessed to approximate values on control surfaces, thereby simplifying the discretization process. Moreover, a residual correction loss term is introduced in this study that significantly accelerates convergence and improves training efficiency. To validate the performance of FFV-PINN, we solve a series of challenging problems — including flow in the two-dimensional steady and unsteady lid-driven cavity, three-dimensional steady lid-driven cavity, backward-facing step scenarios, and natural convection at previously unsurpassed Reynolds (Re) number and Rayleigh (Ra) number, respectively — that are typically difficult for PINNs. Notably, the FFV-PINN can achieve data-free solutions for the lid-driven cavity flow at $Re = 10000$ and natural convection at $Ra = 10^8$ for the first time in PINN literature, even while requiring only 680s and 231s respectively. These results further highlight the effectiveness of FFV-PINN in improving both speed and accuracy, marking another step forward in the progression of PINNs as competitive neural PDE solvers.

Keywords: Physics-informed Neural Network, Finite volume method, Residual correction loss, Partial differential equations, Fluid mechanics

1. Introduction

Over the past few years, data-driven models have increasingly demonstrated their utility across various fields (LeCun et al., 2015), including but not limited to computer vision, natural language processing, recommendation systems, and autonomous driving. However, when encountering complex physical systems, models that rely exclusively on data often struggle to accurately capture the underlying governing patterns (Karniadakis et al., 2021). In this context, physics-informed neural networks (PINNs) (Raissi et al., 2019) have emerged as a highly promising and innovative solution. The integration of the representational capacity of neural networks with prior physical knowledge enables PINNs to mitigate a fundamental drawback of purely data-driven models, namely, their reliance on extensive and often impractical datasets. Excitingly, this synergy promises to enhance the model’s capability to solve complex problems with fewer data points, making it particularly suitable for real-world applications where data can be scarce or difficult to obtain. In addition to these advantages, PINNs exhibit remarkable versatility, making them applicable to both forward and inverse problems (Yuan

et al., 2022; Lou et al., 2021). The ability to handle both problem types within a unified framework further extends their applicability across diverse fields including fluid dynamics (Cai et al., 2021), structural mechanics (Hu et al., 2024), climate modeling (Dutta et al., 2024), and biomedical simulations (Sarabian et al., 2022).

However, despite their remarkable potential across a wide range of physical problems, PINNs encounter several challenges that impede their broader development and practical implementation (Wang et al., 2022b). A primary limitation stems from their relatively weak enforcement of physical constraints (Chiu et al., 2022; Wei et al., 2025). Specifically, the loss function in PINNs is typically formulated using automatic differentiation (AD) by solely computing the residuals of the governing equations at isolated collocation points (Raissi et al., 2019). While AD is simple and straightforward to implement, it does not incorporate information from adjacent points, thereby neglecting the conservation relationships that exist among them (Karnakov et al., 2024). When PINNs fail to account for these relationships, the resulting solutions may violate fundamental physical principles (Jagtap et al., 2020), particularly in complex scenarios where interactions among points play a critical role. Although increasing the number of collocation points may improve the model’s adherence to physical laws and enhance solution accuracy, this strategy incurs significantly higher computational costs and longer training times.

Several strategies have been proposed to enhance the conservation properties of PINNs. For instance, the conservative PINN (cPINN) (Jagtap et al., 2020) employs domain decomposition with interfacial flux conservation; however, this approach may suffer from interface errors that impair training stability and solution accuracy. Alternatively, two-stage PINNs (Lin and Chen, 2022) attempt to improve conservation by incorporating the mean square error of conserved quantities into the loss function, and this idea has been further refined into a single-stage formulation using adaptive weighting techniques (Wang et al., 2022a). The PINN-Proj model (Baez et al., 2024) enforces conservation by projecting the network output onto a conservation-adhering function space, albeit limited to systems with zero net flux. Other approaches include Continuity Planes and Monte Carlo integration (Gurieva et al., 2022), tailored loss functions for solitons (Wu et al., 2022), and direct integration of integral conservation laws via finite volume methods (Hansen et al., 2023). Integral formulations have also been explored, either by predicting integral quantities directly (Rajvanshi and Ketcheson, 2024) or by

embedding weak-form representations into the loss via coupled neural networks (Wang and Yang, 2024). Nevertheless, many of these methods rely on initial conditions for calculating conserved quantities, rendering them unsuitable for steady problems. Furthermore, the complex derivation and computation of conserved quantities often restrict their applicability (Lin and Chen, 2022). Critically, these approaches are predominantly tailored for integrable systems and may not be directly applicable to complex equations such as the Navier-Stokes equations.

Beyond the aforementioned issue, PINNs frequently encounter challenges pertaining to instability and poor convergence during training (Fabiani et al., 2024; Cuomo et al., 2022). The optimization landscape for PINNs is highly non-convex, complicating the training process and inducing oscillations in the loss function. Such instability can severely impede the model’s ability to achieve convergence towards a stable solution, especially in complex fluid dynamics problems characterized by highly nonlinear dynamics. Consequently, more efficient strategies must be developed to strengthen physical constraints while ensuring computational stability and convergence.

Recently, increasing researchers (Lim et al., 2022; Xiang et al., 2022; Chiu et al., 2022; Jiang et al., 2023; Xiao et al., 2024; Cen and Zou, 2024; Mei et al., 2024; Su et al., 2024; Zhang et al., 2025; Zhu et al., 2024) have explored the integration of traditional numerical methods, such as the finite difference method (FDM) (Thomas, 2013) and the finite volume method (FVM) (Patankar, 2018), within the PINN framework to mitigate the issue of weak physical constraint enforcement. These approaches leverage well-established numerical methods (Malalasekera, 2007) to approximate the derivative terms in the partial differential equations (PDEs) using discretization schemes, thereby enhancing the spatial relationship across collocation points. For example, Xiang et al. (Xiang et al., 2022) proposed a hybrid finite difference physics-informed neural network (HFD-PINN) framework, wherein FDM was applied locally to replace AD within the PINN framework, thereby effectively balancing computational efficiency and accuracy. Zhang et al. (Zhang et al., 2025) further proposed a physics-informed graph neural network based on the finite volume method (FVGP-Net) for the unsupervised training and prediction of steady incompressible laminar convective heat transfer problems. Chiu et al. (Chiu et al., 2022) also proposed to couple AD with a numerical scheme for loss construction, resulting in fast and sample-efficient PINNs.

Concurrently, researchers have proposed various methods and strategies,

such as adaptive training techniques (Katende et al., 2024; Fabiani et al., 2024; Meng et al., 2024; Jahani-Nasab and Bijarchi, 2024; Rathore et al., 2024), modified loss function formulations (Meng et al., 2023; Hu et al., 2023; Nosrati and Emami Niri, 2024), as well as advanced neural network architectures (Kaplarević-Mališić et al., 2023; Wang and Zhong, 2024; Moser et al., 2023), to address inherent challenges of stability and convergence when training PINNs in the AD framework. For instance, McClenny et al. (McClenny and Braga-Neto, 2023) improved model stability by optimizing the physical residual weights in the loss function through adaptive weighting strategies.

Despite these advancements, challenges remain in ensuring the conservation constraints are adequately satisfied throughout the training process and in maintaining the model’s stability and convergence. Firstly, existing hybrid frameworks, which integrate PINNs with traditional numerical methods, frequently encounter numerical instability when discretizing convection terms. This instability manifests as pronounced dispersion and dissipation errors, which not only compromise the accuracy of the solutions but also substantially obstruct the effective enforcement of physical constraints. As a result, these models struggle to accurately capture complex physical phenomena (Wang et al., 2023b; Jiang et al., 2023). Secondly, prevailing strategies for enhancing the convergence and stability of PINNs predominantly adopt machine learning methods, emphasizing algorithmic or architectural improvements while giving insufficient attention to the physical constraints. This limited incorporation of physical information into the optimization process restricts the model’s stability and convergence, particularly in complex physical scenarios.

To address the aforementioned limitations, this paper introduces a fast finite volume physics-informed neural network framework, referred to as FFV-PINN (schematic in Fig. 1), which integrates a simplified FVM to enhance the imposition of physical constraints and a novel residual correction loss to enable fast and stable training. Specifically, the simplified FVM is proposed to improve numerical stability, thereby facilitating the better enforcement of physical constraints. Distinct from traditional FVM, where discretization schemes for convective terms are selected based on the direction of the convection, as well as the relative magnitudes of convection and diffusion (Tao, 2021), FFV-PINN bypasses this tedious step by utilizing neural network outputs to directly approximate values on the control surfaces. In this way, the FFV-PINN can improve the dispersion and dissipation behavior while significantly simplifying the discretization process. In the mean-

time, the novel residual correction loss is designed from the perspective of physical constraints to enhance the convergence and stability of the neural network during training. By acting as a guiding mechanism for parameter updates, this loss term ensures that the network’s outputs remain closely aligned with established conservation principles. To evaluate FFV-PINN’s performance, a series of canonical fluid dynamics benchmark problems, such as two-dimensional (2D) steady and unsteady lid-driven cavity flows, three-dimensional (3D) steady lid-driven cavity flow, backward-facing step flow, and natural convection phenomena, are investigated. These selected cases are commonly employed in the evaluation of new computational physics algorithms for their respective inherent complexity and associated challenges for numerical methods and serve as rigorous validation of the framework’s predictive capabilities in this work.

Compared to previous studies that enforce conservation laws, the FFV-PINN presents notable advantages. First, by integrating the FVM, which is inherently designed for conservation laws (Hansen et al., 2023), the discretized PDE is directly embedded into the loss function. This allows FFV-PINN to be applied to more intricate systems beyond the limitations of integrable models. Second, the residual correction loss term in FFV-PINN, derived from the conservation equation, offers more effective guidance for neural network parameter updates during training. Furthermore, unlike many existing methods, FFV-PINN does not rely on initial conditions to compute conserved quantities, making it applicable to both steady and unsteady problems.

Our main contributions can be summarized as:

- We propose a simplified FVM to handle the discretization of the convection term within governing equations, resulting in a more streamlined discretization process while maintaining numerical accuracy.
- We introduce a residual correction loss term designed to align the neural network outputs with conservation principles. This innovative loss term not only enforces the physical constraints more effectively but also acts as a guide for updating the neural network parameters, thereby improving the performance of the model and facilitating faster convergence during training.
- The efficacy of FFV-PINN is demonstrated through application to challenging benchmark problems. Notably, data-free solutions for a lid-

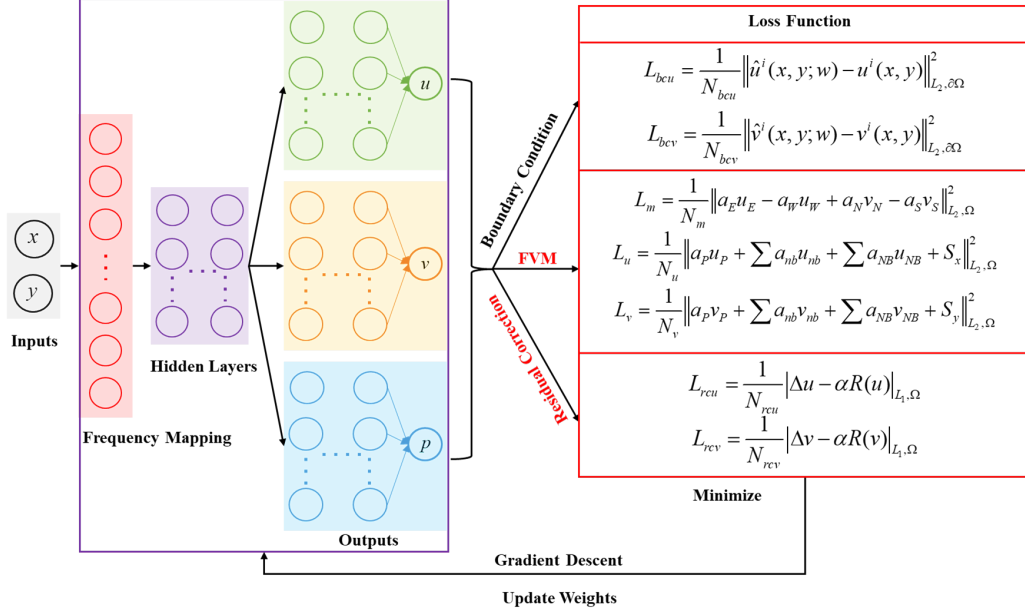


Figure 1: Schematic representation of the proposed FFV-PINN framework integrated with the simplified FVM and residual correction loss. The neural network takes spatial coordinates (x, y) as inputs and predicts velocity components u, v and pressure p . The loss function comprises three components: the BC loss, the physical constraint loss derived from the discretized governing equations, and the residual correction loss, which refines the solution by addressing deviations from the expected physical constraints.

driven cavity flow at high Reynolds number ($Re = 10000$) and a natural convection problem at high Rayleigh number ($Ra = 10^8$) are presented for the first time, demonstrating high accuracy and reduced training time that other PINNs have heretofore been unable to attain.

The remainder of this paper is structured as follows: Section 2 outlines the basic loss formulation of PINNs, proceeds to discuss their integration with numerical discretization techniques, and finally presents the FFV-PINN framework. Section 3 reports extensive experimental studies across multiple benchmark problems, with explicit comparison to existing literature to demonstrate FFV-PINN's advantages. Section 4 offers concluding remarks and outlines potential directions for future research.

2. Methodology

2.1. The overview of PINNs

Without loss of generality, we consider a canonical physics-informed learning problem governed by the following general PDEs:

$$\text{PDE:} \quad \mathcal{N}_\vartheta[u(x, t)] = h(x, t), \quad x \in \Omega, t \in (0, T] \quad (1a)$$

$$\text{IC:} \quad u(x, t = 0) = u_0(x), \quad x \in \Omega \quad (1b)$$

$$\text{BC:} \quad u(x, t) = g(x, t), \quad x \in \partial\Omega, t \in (0, T] \quad (1c)$$

where the input variables are denoted as x and t , representing the spatial and temporal variables respectively, while u represents the output of interest. The general differential operator $\mathcal{N}_\vartheta[u(x, t)]$ contains parameters ϑ that are associated with the PDEs and may include both linear and nonlinear combinations of the temporal and spatial derivatives of the output u . In addition, $h(x, t)$ represents a general source term defined within the domain $x \in \Omega, t \in (0, T]$. The initial condition (IC), as given by Eq. 1b, specifies $u(x, t) = u_0(x)$ at the initial time $t = 0$. Furthermore, Eq. 1c specifies the boundary condition (BC), indicating that $u(x, t)$ is equal to $g(x, t)$ at the boundary of the domain $\partial\Omega$. Here, $g(x, t)$ may be a Dirichlet BC, a Neumann BC, a Robin BC, or any combination thereof.

The loss function of a PINN model is composed of multiple terms, including PDE loss, IC loss, and BC loss.

$$\mathcal{L} = \lambda_{pde} \mathcal{L}_{pde} + \lambda_{ic} \mathcal{L}_{ic} + \lambda_{bc} \mathcal{L}_{bc} \quad (2a)$$

$$\mathcal{L}_{pde} = \frac{1}{N_{pde}} \|\mathcal{N}_\vartheta[f(\cdot; \mathbf{w})] - h(\cdot)\|_{L_2(\Omega \times (0, T])}^2 \quad (2b)$$

$$\mathcal{L}_{ic} = \frac{1}{N_{ic}} \|f(\cdot, t = 0; \mathbf{w}) - u_0(\cdot)\|_{L_2(\Omega)}^2 \quad (2c)$$

$$\mathcal{L}_{bc} = \frac{1}{N_{bc}} \|\mathcal{B}[f(\cdot; \mathbf{w})] - g(\cdot)\|_{L_2(\partial\Omega \times (0, T])}^2 \quad (2d)$$

where $f(\cdot; \mathbf{w})$ represents the output function of the PINN as parameterized by the network weights \mathbf{w} , and evaluated over a set of unlabeled collocation points sampled from the spatiotemporal domain. The weighting factors, λ , serve to balance the magnitude of different loss terms. The N_{pde} , N_{ic} , and N_{bc} represent the number of training collocation points used for enforcing the PDE residual, initial conditions, and boundary conditions, respectively. The $\|\cdot\|_{L_2}$ represents the L_2 norm, which is used to quantify the magnitude of the loss terms.

2.2. Integration of PINNs with numerical methods

While PINNs can exactly calculate the derivative terms in PDEs on a set of collocation points by AD, they fail to exploit potential properties that are both physically and numerically motivated (Karnakov et al., 2024). These properties, common in well-established numerical methods, are advantageous for enhancing the overall model performance. In particular, the integral conservation property inherent in the FVM offers a way to reinforce the physical constraints within PINNs, maintaining its validity irrespective of grid resolution (Patankar (2018)). Therefore, this study adopts FVM to exemplify its integration with PINNs, illustrating the potential benefits of such a hybridized approach.

2.2.1. Hybrid framework combining PINN with FVM

Taking the 2D steady lid-driven cavity flow problem presented in Section 3 as an example, the underlying physical laws are described by the 2D steady incompressible Navier–Stokes (N-S) equations:

$$\frac{\partial u}{\partial x} + \frac{\partial v}{\partial y} = 0 \quad (3a)$$

$$\frac{\partial (uu)}{\partial x} + \frac{\partial (vu)}{\partial y} = \frac{1}{Re} \left(\frac{\partial^2 u}{\partial x^2} + \frac{\partial^2 u}{\partial y^2} \right) - \frac{\partial p}{\partial x} \quad (3b)$$

$$\frac{\partial (uv)}{\partial x} + \frac{\partial (vv)}{\partial y} = \frac{1}{Re} \left(\frac{\partial^2 v}{\partial x^2} + \frac{\partial^2 v}{\partial y^2} \right) - \frac{\partial p}{\partial y} \quad (3c)$$

where Re denotes the Reynolds number, a dimensionless quantity in fluid mechanics that can indicate the complexity of flow behavior. Let the dependent variable of interest within the momentum equations (Eqs. 3b and 3c) be designated as ϕ . A general differential equation can then be formulated, encompassing the convection, diffusion, and source terms:

$$\frac{\partial (u\phi)}{\partial x} + \frac{\partial (v\phi)}{\partial y} = \frac{1}{Re} \left(\frac{\partial^2 \phi}{\partial x^2} + \frac{\partial^2 \phi}{\partial y^2} \right) + S \quad (4)$$

Here, the dependent variable ϕ represents the velocity components u and v in the x -direction and y -direction, respectively. The source term S corresponds to the pressure gradient, specifically $-\frac{\partial p}{\partial x}$ for x -direction and $-\frac{\partial p}{\partial y}$ for y -direction, respectively.

Performing a volume integral of Eq. 4 over the control volume ($\Delta x = \Delta y$) illustrated in Fig. 2 yields the integral conservation form. This formulation embodies the fundamental principle of physical quantity conservation, applicable to

quantities such as momentum or energy, within the defined control volume V :

$$\int_V \left(\frac{\partial(u\phi)}{\partial x} + \frac{\partial(v\phi)}{\partial y} \right) dV = \int_V \frac{1}{Re} \left(\frac{\partial^2 \phi}{\partial x^2} + \frac{\partial^2 \phi}{\partial y^2} \right) dV + \int_V S dV \quad (5)$$

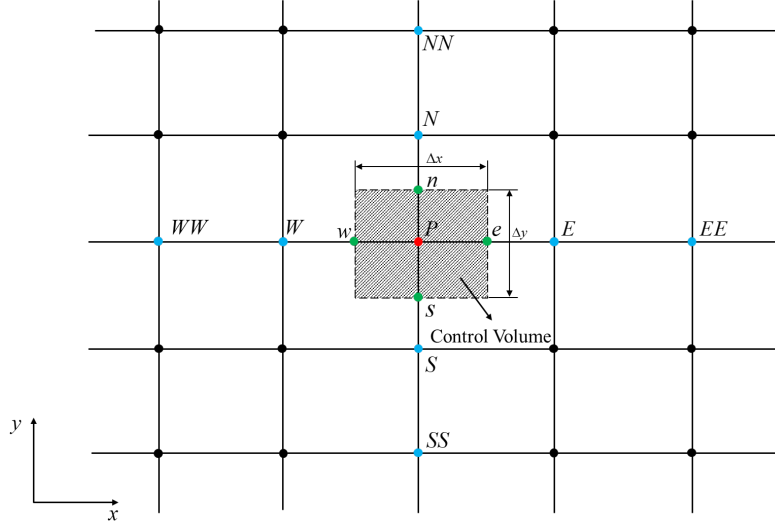


Figure 2: Control volume for the 2D domain. The capital letters (E , W , N , S , EE , WW , NN and SS) denote the surrounding nodes, while the lowercase letters (e , w , n and s) represent the control surfaces. The capital letter P refers to the center of the control volume. For simplicity of illustration, the spacing between adjacent grid points in both the x -direction and the y -direction is kept equal, with $\Delta x = \Delta y$, but this is not a necessity.

In the traditional FVM, the diffusion term is typically discretized using the central difference (CD) scheme, which offers a simple and effective method for approximating second-order spatial derivatives (Patankar, 2018; Malalasekera, 2007; Darwish, 2016). The diffusion term in Eq. 5 is discretized approximately as follows:

$$\int_V \frac{1}{Re} \left(\frac{\partial^2 \phi}{\partial x^2} + \frac{\partial^2 \phi}{\partial y^2} \right) dV \approx \frac{1}{Re} (\phi_E + \phi_W + \phi_N + \phi_S - 4\phi_P) \quad (6)$$

Subsequently, the source term in the x -direction and y -direction can be discretized as follows:

$$\int_V -\frac{\partial p}{\partial x} dV \approx \frac{-(p_E - p_W) \Delta y}{2} \quad (7a)$$

$$\int_V -\frac{\partial p}{\partial y} dV \approx \frac{-(p_N - p_S) \Delta x}{2} \quad (7b)$$

Furthermore, volume integration of the convection term is carried out:

$$\int_V \frac{\partial(u\phi)}{\partial x} dV = \int_s^n \int_w^e \frac{\partial(u\phi)}{\partial x} dx dy \approx [(u\phi)_e - (u\phi)_w] \Delta y \quad (8)$$

We introduce a new symbol F , defined as $F = u\Delta y$, which represents the strength of the convection. Hence, Eq. 8 can be expressed as:

$$[(u\phi)_e - (u\phi)_w] \Delta y = (F\phi)_e - (F\phi)_w \quad (9)$$

A variety of discretization schemes are available for approximating the convection term. Taking ϕ_e as example, the following discretization can be derived:

- **Central difference (CD) scheme**

$$\phi_e = \frac{\phi_E + \phi_W}{2} \quad (10)$$

- **First order upwind (FOU) scheme**

$$\phi_e = \begin{cases} \phi_P, & F_e \geq 0 \\ \phi_E, & \text{otherwise} \end{cases} \quad (11)$$

- **Second order upwind (SOU) scheme**

$$\phi_e = \begin{cases} \frac{3}{2}\phi_P - \frac{1}{2}\phi_W, & F_e \geq 0 \\ \frac{3}{2}\phi_E - \frac{1}{2}\phi_{EE}, & \text{otherwise} \end{cases} \quad (12)$$

By substituting the aforementioned discretized forms of the convection term, diffusion term, and source term into Eq. 5, we derive the following general discretized equation:

$$a_P\phi_P + \sum a_{NB}\phi_{NB} + b = 0 \quad (13)$$

where a_P is the coefficient associated with the central node P , a_{NB} represents the coefficients of the neighboring nodes NB (comprising E, W, N, S, EE, WW, NN , and SS), and b is the source term. Within the framework that integrates PINNs with the FVM, the PDE-based physical loss (L_{pde}) is transformed into a physical loss based on the discretized equation (L_{de}). Specifically, the physical loss term imposed by the momentum equation is expressed as follows:

$$\mathcal{L}_{de} = \frac{1}{N_{de}} \|a_P\phi_P + \sum a_{NB}\phi_{NB} + b\|_{L_2(\Omega \times (0,T))}^2 \quad (14)$$

Comparing Eq. 14 with Eq. 2b, it can be observed that the loss term based on the discretized equation establishes an algebraic relationship between the collocation point and its surrounding nodes, enabling a more effective imposition of physical constraints.

2.3. The FFV-PINN framework

2.3.1. The simplified FVM

A variety of discretization schemes exist for the convection term, including FOU, CD, and SOU, among others. The appropriate choice of discretization scheme typically depends on the direction of the convection or the relative magnitudes of convection and diffusion strength. In convection-dominated flows, upwind schemes are frequently favored to ensure numerical stability and capture the directional nature of convective transport. Conversely, in diffusion-dominated flows, the CD scheme is generally considered more suitable. It is therefore apparent that the selection of a discretization scheme for the convection term is a non-trivial task that requires a thorough understanding of the underlying physical phenomena and the strengths and limitations of different numerical methods.

Given the complexities associated with this decision-making process, a more robust discretization scheme for the convection term is needed in the context of PINNs. To this end, we introduce a simplified FVM, which leverages the neural network's ability to produce outputs at arbitrary positions. The discretized form of the convection term denoted as Eq. 8, can then be implemented directly without requiring further discretization for cell-face velocity. As a result, the integral form of convective term $\frac{\partial(v\phi)}{\partial y}$, when discretized in the control volume depicted in Fig. 2, results in the following expression:

$$\int_V \frac{\partial(v\phi)}{\partial y} dV \approx [(v\phi)_n - (v\phi)_s] \Delta x \quad (15)$$

The simplified FVM enhances the flexibility and efficiency of the discretization process, mitigating the inherent complexities typically associated with traditional FVM. Moreover, the proposed scheme exhibits superior dispersion and dissipation properties based on theoretical analysis detailed in Section 2.4.

By systematically organizing the discretized forms of the convection term, diffusion term, and source term, we arrive at the following expression:

$$a_P\phi_P + \sum a_{NB}\phi_{NB} + \sum a_{nb}\phi_{nb} + b = 0 \quad (16)$$

where the a_P represents the coefficient associated with the central node P , a_{NB} denotes the coefficients corresponding to the neighboring nodes NB (each of E , W , N , S) surrounding the given control volume, and a_{nb} refers to the coefficients associated with the control faces nb (e , w , n , s) of a given control volume. The detailed coefficients can be found in Appendix A. Therefore, the physical constraints derived from the momentum equation can be re-formulated as follows:

$$\mathcal{L}_{de} = \frac{1}{N_{de}} \|a_P\phi_P + \sum a_{NB}\phi_{NB} + \sum a_{nb}\phi_{nb} + b\|_{L_2(\Omega \times (0,T])}^2 \quad (17)$$

It is worth noting that, through discretization, conservation laws are naturally incorporated into the loss function in the form of physics-informed constraints. Theoretically, if the training points, which are uniformly distributed, fully cover the computational domain and the loss function converges to zero, FFV-PINN can exactly satisfy global conservation laws. In practice, however, mini-batch training is adopted due to computational limitations, leading to the local enforcement of conservation. Although conservation is enforced only at the local level, these constraints cumulatively lead to an accurate approximation of global conservation as training progresses and the loss decreases. The subsequent numerical experiments in Section 3 further verify that FFV-PINN outperforms traditional AD-based PINNs in terms of both accuracy and computational efficiency, thereby demonstrating its effective compatibility with conservation laws.

2.3.2. Residual correction loss

Having established the physical constraints based on FVM, it is now pertinent to highlight the fundamental differences in how PINNs and FVM obtain the solution of PDEs. Whereas FVM relies on constructing a linear system to solve PDEs directly or iteratively, PINNs instead provide a markedly distinct paradigm by recasting a numerical problem as an optimization problem. Specifically, the neural network adjusts its parameters by minimizing a defined loss function, with the objective of reducing each loss term as close to zero as possible. This optimization constitutes the core of the neural network’s training process. Consequently, to enforce compliance with the governing equations, PINNs are designed to minimize the physics-based loss term, defined in Eq. 17, with the ideal target of achieving zero. However, it is critical to acknowledge the distinction between theoretical ideal and practical reality. While perfect convergence, in theory, would indeed reduce this term to zero, practical implementations invariably yield finite residuals, denoted as r^n at the training epoch n . The residuals quantitatively represent the extent of the current solution’s deviation from the governing equations, and this is formalized as follows:

$$a_P \phi_P^n + \sum a_{NB} \phi_{NB}^n + \sum a_{nb}^n \phi_{nb}^n + b^n = r^n \quad (18)$$

The coefficients a_P and a_{NB} are predetermined based on the discretization scheme and the physical properties of the system as detailed in Eq.A.1. Critically, these coefficients remain constant and unaffected by neural network parameter updates. Let us now assume the physical constraints are met in the subsequent update step—the $(n + 1)$ -th epoch. Under this assumption, the physics loss is expressed as follows:

$$a_P \phi_P^{n+1} + \sum a_{NB} \phi_{NB}^{n+1} + \sum a_{nb}^{n+1} \phi_{nb}^{n+1} + b^{n+1} = 0 \quad (19)$$

By subtracting Eq. 18 from Eq. 19, the subsequent expression is derived:

$$\sum (a_{nb}^{n+1}\phi_{nb}^{n+1} - a_{nb}^n\phi_{nb}^n) + \sum a_{NB} (\phi_{NB}^{n+1} - \phi_{NB}^n) + a_P (\phi_P^{n+1} - \phi_P^n) + (b^{n+1} - b^n) = -r^n \quad (20)$$

By rearranging Eq. 20, we can obtain:

$$\phi_P^{n+1} - \phi_P^n = \frac{-r^n - \sum (a_{nb}^{n+1}\phi_{nb}^{n+1} - a_{nb}^n\phi_{nb}^n) - \sum a_{NB} (\phi_{NB}^{n+1} - \phi_{NB}^n) - (b^{n+1} - b^n)}{a_P} \quad (21)$$

When the update of ϕ_P^n is equal to Eq. 21, this implies the physical constraints within the neural network are satisfied. The adjustments applied to the predictions are not arbitrary but systematically derived from discrepancies identified in the current prediction. This relationship is essential for ensuring that the model learns effectively and converges to a solution that adheres to the physical laws governing the system.

Inspired by the SIMPLE algorithm (Patankar, 2018) in the FVM, we propose a modification to Eq. (21) by neglecting the term $\sum (a_{nb}^{n+1}\phi_{nb}^{n+1} - a_{nb}^n\phi_{nb}^n)$. This simplification facilitates implementation and improves model efficiency. As a result, we obtain the following approximation:

$$\phi_P^{n+1} - \phi_P^n \approx R = \frac{-r^n - \sum a_{NB} (\phi_{NB}^{n+1} - \phi_{NB}^n) - (b^{n+1} - b^n)}{a_P} \quad (22)$$

where R is defined as the residual correction term. As discussed in the SIMPLE algorithm (Patankar, 2018), neglecting the contributions from neighboring nodes may lead to overestimating the correction terms. Therefore, to mitigate this issue and enhance the stability of the training process, we introduce α , a relaxation factor for the residual correction to modulate the influence of R , leading to the following expression:

$$\phi_P^{n+1} = \phi_P^n + \alpha R \quad (23)$$

To correct the update behavior of the neural network, we define the residual correction loss term L_{rc} using the L_1 norm as:

$$L_{rc} = \frac{1}{N_{rc}} |\phi_P^{n+1} - \phi_P^n - \alpha R|_{L_1(\Omega \times (0, T])} \quad (24)$$

Since the value at the $(n+1)$ -th epoch is not directly available during training, we estimate it using a second-order extrapolation scheme, given by:

$$\phi^{n+1} = 2\phi^n - \phi^{n-1} \quad (25a)$$

$$b^{n+1} = 2b^n - b^{n-1} \quad (25b)$$

Substituting Eq. (25) into Eq. (24), we simplify the loss term as:

$$L_{rc} = \frac{1}{N_{rc}} \left| \phi_P^n - \phi_P^{n-1} - \alpha R \right|_{L_1(\Omega \times (0, T])} \quad (26)$$

where R is now expressed as:

$$R = \frac{-r^n - \sum a_{NB} (\phi_{NB}^n - \phi_{NB}^{n-1}) - (b^n - b^{n-1})}{a_P} \quad (27)$$

The optimal choice of α is inherently problem-dependent and lacks a universal selection criterion (Moukalled et al., 2016). It is typically determined through empirical tuning and is influenced by factors such as the problem type, neural network architecture, and the number of collocation points. Although α can be individually tailored for different variables, for simplicity and to minimize parametric complexity in the FFV-PINN framework, the same relaxation factor is applied to all variables.

It is noted that the newly proposed residual correction loss term plays a crucial role in directing the training trajectory of the neural network. It theoretically guarantees that updates are executed in a manner concordant with the fulfillment of physical constraints. The underlying rationale for establishing the residual correction is that R quantifies the difference between predicted values and perfect converged, physics-consistent outcomes, as estimated by the last two epochs.

In summary, the proposed FFV-PINN framework, as illustrated in Fig. 1, incorporates two essential losses in addition to the BC loss: the physical constraint loss (Eq. 17), which ensures adherence to physical laws, and the residual correction loss (Eq. 24), which minimizes model residuals to enhance convergence and stability. These loss terms are carefully designed to enhance model performance, ensuring predictive accuracy via adherence to the underlying physical principles governing the system.

2.4. Fundamental analysis

We further analyze the dispersion and dissipation properties of the proposed discretization scheme for the convection term. To this end, Fourier analysis is employed. Assuming the field variable is denoted as ϕ , its Fourier transform and inverse transform can be expressed as follows.

- **Fourier Transform:**

$$\hat{\phi}(k) = \frac{1}{2\pi} \int_{-\infty}^{\infty} \phi(x) e^{-ikx} dx \quad (28)$$

- **Inverse Fourier Transform:**

$$\phi(x) = \frac{1}{2\pi} \int_{-\infty}^{\infty} \hat{\phi}(k) e^{ikx} dk \quad (29)$$

where k represents the wavenumber, and x is the spatial coordinate, i denotes the imaginary unit. For the simplified FVM, the spatial derivative $\frac{\partial\phi}{\partial x}$ can be mathematically represented as follows:

$$\frac{\partial\phi}{\partial x} = \frac{\phi_e - \phi_w}{h} = \frac{\phi(x + \frac{h}{2}) - \phi(x - \frac{h}{2})}{h} \quad (30)$$

where $h = \Delta x$, and ϕ_e and ϕ_w are obtained directly by the neural network.

Subsequently, the Fourier transform is applied to Eq. 30.

$$ikh\hat{\phi}(k) = e^{i\frac{kh}{2}}\hat{\phi}(k) - e^{-i\frac{kh}{2}}\hat{\phi}(k) \quad (31)$$

Through manipulation of the aforementioned equation, the following is derived:

$$ikh = e^{i\frac{kh}{2}} - e^{-i\frac{kh}{2}} \quad (32)$$

Under the approximation that the effective wavenumber $k' \cong k$, and multiplying both sides of the above equation by $-i$, we can deduce:

$$k'h = -i \left(e^{i\frac{kh}{2}} - e^{-i\frac{kh}{2}} \right) \quad (33)$$

The real and imaginary parts of Eq. 33 can be further simplified as:

$$\Re(k'h) = \Re \left[-i \left(e^{i\frac{kh}{2}} - e^{-i\frac{kh}{2}} \right) \right] = 2 \sin \left(\frac{kh}{2} \right) \quad (34a)$$

$$\Im(k'h) = \Im \left[-i \left(e^{i\frac{kh}{2}} - e^{-i\frac{kh}{2}} \right) \right] = 0 \quad (34b)$$

The dispersion (κ_i) and dissipation (κ_r) can be defined as:

$$\kappa_i = \Re(k'h) \quad (35a)$$

$$\kappa_r = \Im(k'h) \quad (35b)$$

Fig. 3 compares the proposed scheme with established schemes (CD, FOU, and SOU) by analyzing the relationship between kh , κ_i and $|\kappa_r|$. This comparison also yields insight into the fundamental dispersion and dissipation characteristics of each scheme. A detailed fundamental analysis of the established schemes is provided in Appendix B. As demonstrated in Fig. 3, the proposed scheme closely matches the exact solution in terms of dispersion. It outperforms other schemes like FOU and SOU, which exhibit significant deviations from the exact solution,

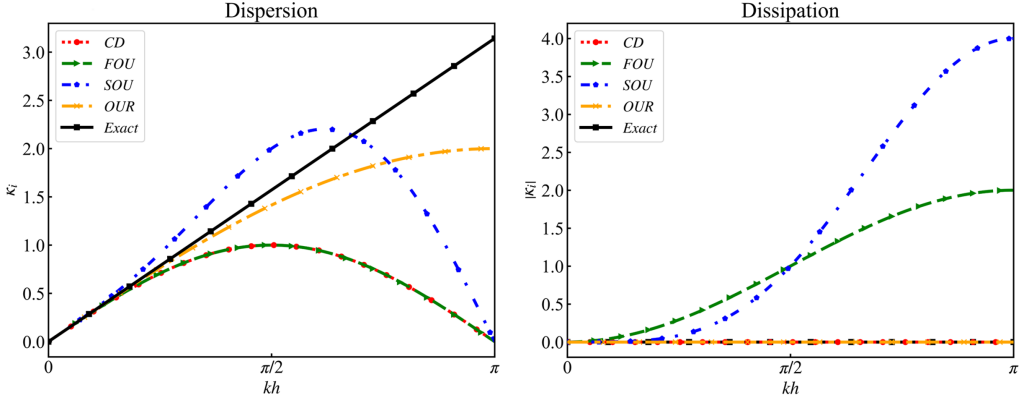


Figure 3: Comparison of the dispersion and dissipation characteristics of each scheme.

especially in the high-frequency range. Another key advantage of the proposed scheme is its zero-dissipation property. This non-dissipative characteristic ensures that higher frequency components of the solution can be better captured. Consequently, the fundamental analysis suggests that the developed scheme exhibits superior numerical properties compared to existing methods, even without considering its simpler implementation.

3. Numerical experiments

In this section, we conduct a series of numerical experiments, including 2D steady and unsteady lid-driven cavity flows, 3D steady lid-driven cavity flow, backward-facing step flow, and natural convection in a unit square. The selected benchmark problems are well-known in the fluid dynamics community for their complex nonlinear dynamics and challenging characteristics. By conducting these experiments, we illustrate the advantages of FFV-PINN in terms of stability, convergence, and accuracy relative to other PINNs.

To enhance the network’s capability in capturing high-frequency information, a frequency mapping layer is introduced, where the input coordinates (x, y) are transformed into a high-dimensional space, as illustrated in Fig. 1. For unsteady problems, the temporal coordinate t is included, and the mapping is performed on the input coordinates (t, x, y) . Similarly, for 3D problems, the spatial coordinate z is considered, and the mapping is applied to the coordinates (x, y, z) . Furthermore, to augment the network’s expressive capacity, the architecture employs both shared and variable-specific hidden layers. Specifically, two shared hidden layers are utilized, followed by three variable-specific hidden layers dedicated to the velocity components u , v , and pressure p , respectively. Each hidden layer consists

of 32 neurons and employs the SiLU (Sigmoid Linear Unit) function as the activation function. In 3D problems and natural convection problems, additional output branches are incorporated to represent the velocity component w and the temperature field T , respectively. The neural network is trained using the Adam optimizer, with the learning rate following a warmup cosine decay schedule. All implementations are developed using the JAX library and executed on a single NVIDIA RTX 3090 GPU card.

Table 1 presents a list of additional parameter configurations used in the numerical experiments, including details on batch size, maximum iterations, initial learning rates, weights for each loss term, relaxation factors, and warmup steps. It should be emphasized that all parameters listed in the table were determined empirically or through a process of trial and error, without the application of rigorous hyperparameter optimization techniques. The primary objective of this study is to demonstrate the validity and advantages of the proposed method itself, as opposed to the exhaustive optimization of hyperparameters to achieve optimal performance.

In the remaining numerical experiments presented in this study, α was varied between 0.7 and 0.98. For real-world systems where the true solution remains unknown, we recommend determining α by carefully monitoring the loss function during the training process. Specifically, an appropriate value of α typically manifests as a stable and consistent decrease in the loss function. Conversely, an unsuitable α may lead to oscillations, slow convergence, or even divergence of the loss. Consequently, observing the trajectory of the loss function provides a crucial empirical indicator for assessing the suitability of a chosen α for a given problem. Furthermore, the emergence of meta-learning techniques offers a promising avenue for automating this search (Zoph and Le, 2016; Finn et al., 2017), a direction we intend to explore in our future research.

To quantitatively evaluate the accuracy of the FFV-PINN, this study utilizes two primary metrics: the mean squared error (MSE) and the relative L_2 error. These metrics are essential in quantifying the discrepancies between the model’s predicted solutions and the corresponding numerical (or benchmark) solutions. The MSE is defined as the average of the square of differences between the predicted and actual values. Mathematically, it is expressed as:

$$\text{MSE} = \frac{1}{N} \sum_{i=1}^N (y_i - \hat{y}_i)^2 \quad (36)$$

where y_i represents the actual values from the numerical solution, \hat{y}_i denotes the predicted values from the FFV-PINN model, and N is the total number of data points.

Table 1: Training configurations used in the numerical experiments for five benchmark problems: 2D steady lid-driven cavity (LDC) flow ($Re = 5000$), 2D unsteady LDC flow ($Re = 400$), 3D steady LDC flow ($Re = 1000$), backward-facing step (BFS) flow ($Re = 600$), and natural convection (NC) problem ($Ra = 10^8$). The batch size is calculated as $k_{de} \times N_{de}$, $k_{bc} \times N_{bc}$, and $k_{ic} \times N_{ic}$ (for unsteady cases), where N_{de} , N_{bc} , and N_{ic} represent the number of training points used for physical constraints, boundary conditions, and initial conditions, respectively. The coefficients k_{de} , k_{bc} , and k_{ic} denote the corresponding sampling ratios. Other key parameters include the maximum iterations (Max iter.), initial learning rate (Init. LR), and relaxation factor (Relax. factor).

Parameter	LDC			BFS	NC
	2D steady $Re = 5000$	2D unsteady $Re = 400$	3D steady $Re = 1000$	$Re = 600$	$Ra = 10^8$
Batch size	$0.1 \times N_{de}$ $0.1 \times N_{bc}$ -	$0.01 \times N_{de}$ $0.05 \times N_{bc}$ $0.01 \times N_{ic}$	$0.001 \times N_{de}$ $0.001 \times N_{bc}$ -	$0.1 \times N_{de}$ $0.1 \times N_{bc}$ -	$0.1 \times N_{de}$ $0.1 \times N_{bc}$ -
Weights (λ_i)	$\lambda_{de} = 1$ $\lambda_{bc} = 1$ - $\lambda_{rc} = 5$	$\lambda_{de} = 1$ $\lambda_{bc} = 1$ $\lambda_{ic} = 1$ $\lambda_{rc} = 10$	$\lambda_{de} = 1$ $\lambda_{bc} = 1$ - $\lambda_{rc} = 1$	$\lambda_{de} = 8$ $\lambda_{bc} = 1$ - $\lambda_{rc} = 1$	$\lambda_{de} = 1$ $\lambda_{bc} = 1$ - $\lambda_{rc} = 1$
Max iter.	50000	50000	100000	50000	50000
Init. LR	1e-3	1e-3	1e-3	5e-3	5e-3
Relax. factor	0.79	0.94	0.8	0.97	0.84
Warmup steps	0	0	0	7500	15000

The relative L_2 error provides a normalized measure of the discrepancy between the predicted and actual values, facilitating an assessment of the model’s performance relative to the magnitude of the true solution. Mathematically, it is defined as:

$$\text{Relative } L_2 \text{ error} = \frac{\|y - \hat{y}\|_{L_2}}{\|y\|_{L_2}} \quad (37)$$

where $\|y - \hat{y}\|_2$ represents the L_2 norm of the error vector, and $\|y\|_2$ is the L_2 norm of the actual values.

3.1. Lid-driven cavity flow

The lid-driven cavity flow problem has become a benchmark for the validation of emerging numerical methods in computational fluid dynamics, particularly following the seminal work by (Ghia et al., 1982). The problem is defined within a geometrically simple yet physically rich domain: a 2D 1×1 unit square cavity. The fluid is driven by the tangential motion of the top wall, which moves at a constant horizontal velocity of $u_{\text{lid}} = 1$ while maintaining a zero vertical velocity component ($v_{\text{lid}} = 0$), as schematically illustrated in Fig. 4. In addition, a no-slip boundary condition is imposed on the remaining three walls of the cavity. The linear local structure approximation method (Wong et al., 2023) is employed for boundary conditions in this study, except where otherwise noted. The physics laws governing the system are described by the incompressible N-S equations, as expressed in Eq. 3.

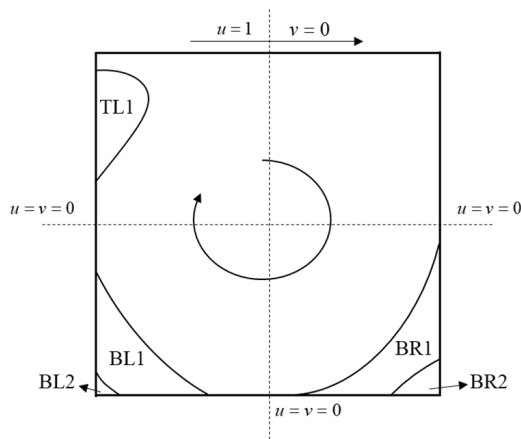


Figure 4: Schematic of the lid-driven cavity problem with key locations marked (TL1, BL1, BL2, BR1, BR2). The top lid moves at a constant velocity ($u = 1, v = 0$), while the other walls are stationary ($u = v = 0$). The central region indicates the expected formation of a recirculating vortex.

The simulation of lid-driven cavity flow at high Re (e.g., $Re = 3200, 5000$) with PINN presents significant challenges. As highlighted in recent studies (Wang et al., 2023a,b, 2024; Cao and Zhang, 2023), PINNs often struggle with training instability and accuracy issues when applied to such problems. Despite these difficulties, our proposed FFV-PINN demonstrates a remarkable ability to maintain both fast convergence and accuracy, as shown in Table 2. Table 2 also summarizes the performance of various PINNs on this benchmark ($Re = 3200, 5000$). Notably, our proposed method outperforms existing approaches, achieving the lowest relative L_2 error. More critically, in comparison to the state-of-the-art SOAP method

(Wang et al., 2025), our approach attains a remarkable reduction in computational cost: while employing a less powerful NVIDIA RTX 3090 GPU (versus the A6000 utilized by SOAP), FFV-PINN achieves a computational speed that is $125\times$ faster than SOAP. These results highlight the FFV-PINN framework’s dual strengths of computational efficiency and accuracy in simulating complex fluid dynamics, even under challenging high Re regimes.

Table 2: Comparison of relative L_2 errors (computed for the velocity components u , v , and the velocity magnitude V) and training time (in *hour*) obtained by different PINNs variants. The computation times of SOAP are provided in the respective paper, while the training time for PirateNet was obtained by running the authors’ provided code on an NVIDIA RTX 3090 GPU card. Additionally, to ensure consistency, we calculated the relative L_2 errors using the benchmark data provided by PirateNet.

References	Re	u	v	V	Time	Hardware
JAXPI (Wang et al., 2023a)	3200	-	-	1.58e-01	-	-
PirateNet (Wang et al., 2024)	3200	-	-	4.21e-02	11.83h	RTX 3090
ev-NSFnet (Wang et al., 2023b)	5000	5.40e-02	5.40e-02	-	-	-
TSONN (Cao and Zhang, 2023)	5000	-	-	1.00e-01	-	-
SOAP (Wang et al., 2025)	5000	-	-	3.99e-02	8.25h	RTX A6000
Ours	3200	3.78e-02	3.72e-02	3.69e-02	0.0636h	RTX 3090
Ours	5000	4.05e-02	4.05e-02	3.90e-02	0.0658h	RTX 3090

To further demonstrate the superior performance of FFV-PINN, we perform training for the lid-driven cavity flow problem at $Re = 7500$ and $Re = 10000$, as shown in Fig. 5 and 6. In both cases, the λ_{de} , λ_{bc} , λ_{rc} , and α are set to 1.0, 1.0, 5.0, and 0.79, respectively. To the best of our knowledge, this represents a groundbreaking achievement: the first successful application of PINNs to this benchmark problem at such high Re numbers without incorporating any data. Particularly noteworthy is the case of $Re = 10000$, where the multiple vortexes with different scales are observed due to highly non-linearity, and also be a challenging problem even using CFD solver (Shankar and Deshpande, 2000).

Fig. 5 shows contours for the lid-driven cavity flow at $Re = 7500$. As shown in the figure, the velocity components (u and v) and the velocity magnitude (V), obtained by the FFV-PINN, exhibit excellent agreement with those computed by high fidelity computational fluid dynamics (CFD) (Chiu, 2018). The contours of the velocity fields from both methods are virtually identical, indicating that the FFV-PINN method accurately captures the complex flow pattern at this high Re . The consistently low absolute error across the computational domain further substantiates this quantitative agreement. Fig. 6 extends this analysis to $Re = 10000$. Despite the increase in Re and nonlinearity, FFV-PINN maintains consistency with the CFD benchmarks. Crucially, unlike prior works (Wang et al., 2023b; Jiang

et al., 2023), which augment PINNs with simulation data to stabilize training, our framework relies exclusively on boundary conditions—no additional training data is employed. This data-free predictive capacity underscores FFV-PINN’s efficiency and distinguishes it from prior PINN work. This also fundamentally expands the potential for FFV-PINN to be applied across a wide array of fluid dynamics applications, especially in problems where the availability of high-quality experimental or simulation data is limited or prohibitive.

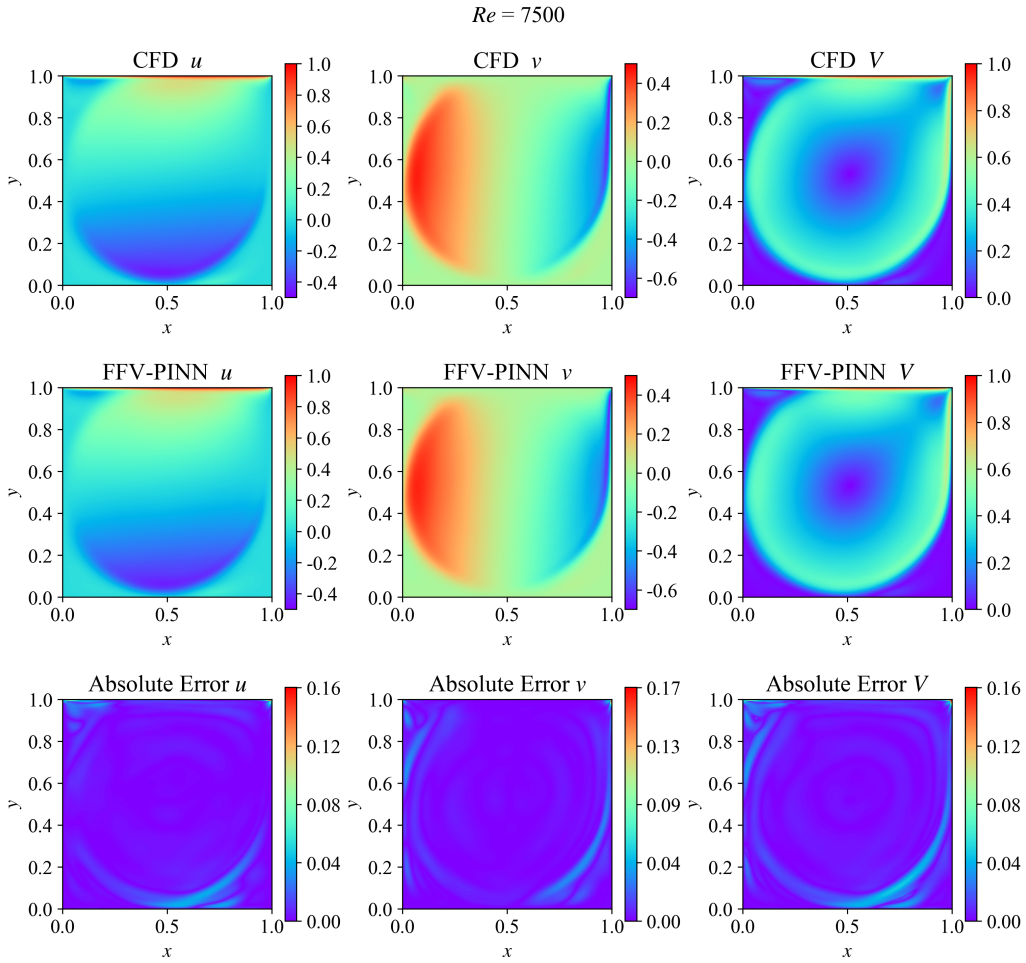


Figure 5: Lid-driven cavity flow at $Re = 7500$. The left column represents the velocity component u , the middle column corresponds to the velocity component v , and the right column depicts the velocity magnitude V . Each row corresponds to, respectively, the solutions obtained via CFD, the proposed FFV-PINN method, and the absolute error between the two.

Fig. 7 displays the streamlines for the lid-driven cavity flow at $Re = 7500$ and $Re = 10000$ respectively. FFV-PINN demonstrates a remarkable ability to replicate the key flow structures that are observed in CFD results. At both Re , FFV-PINN successfully captures the formation of the central primary vortex, which is a dominant feature of the flow pattern within the cavity. Additionally, the model accurately reproduces the secondary corner vortices that develop as a result of the interactions between the fluid and the stationary walls.

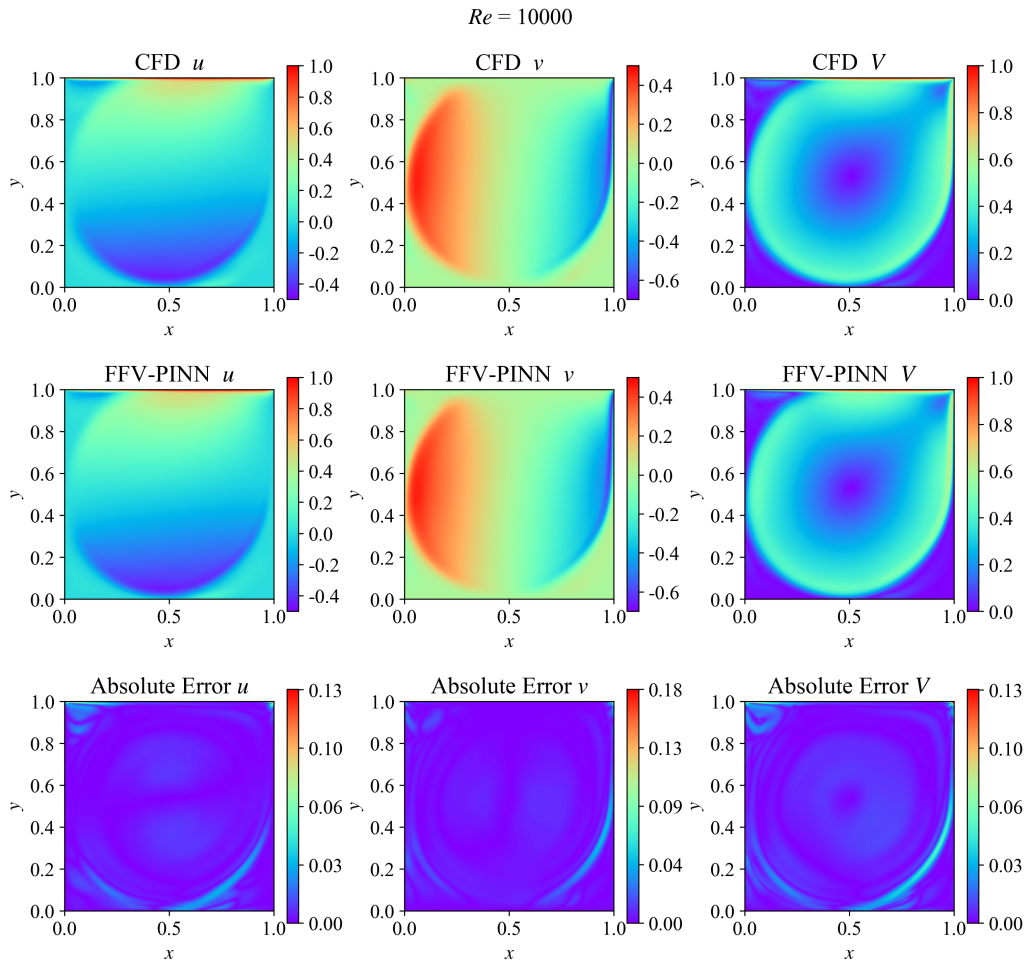


Figure 6: Lid-driven cavity flow at $Re = 10000$. The left column represents the velocity component u , the middle column corresponds to the velocity component v , and the right column depicts the velocity magnitude V . Each row corresponds to, respectively, the solutions obtained via CFD, the proposed FFV-PINN method, and the absolute error between the two.

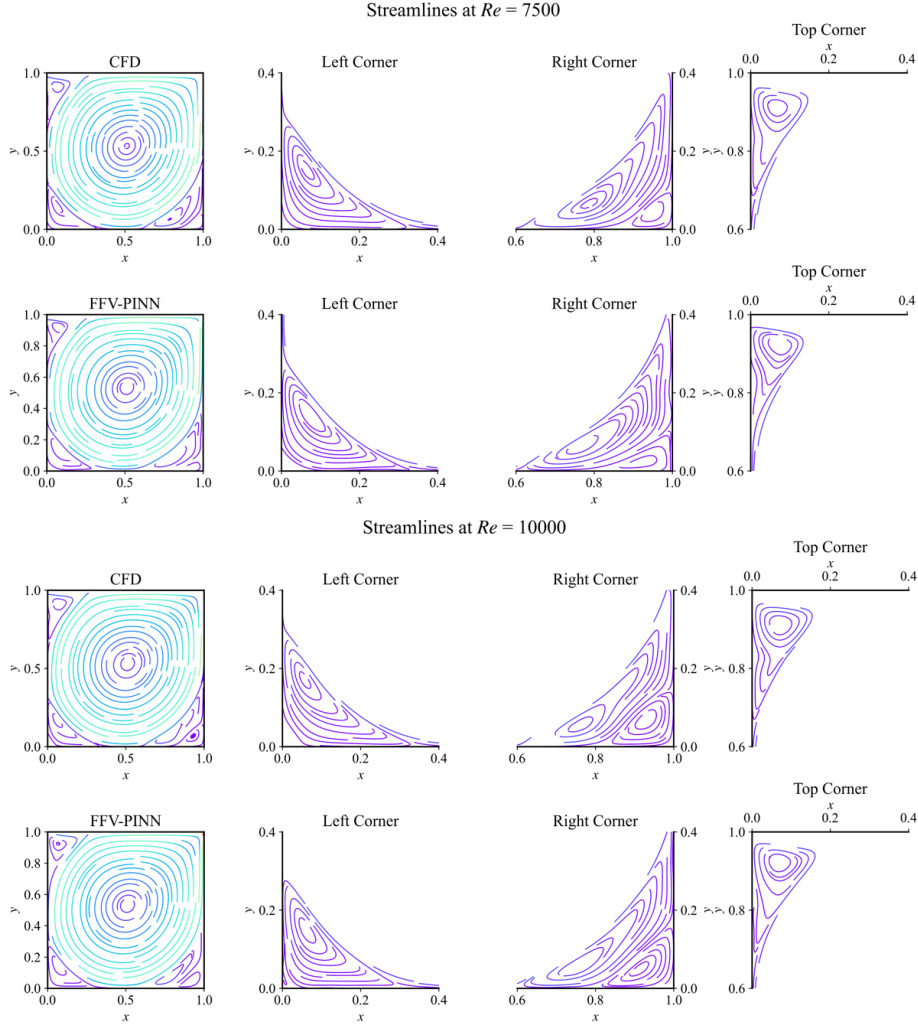


Figure 7: Streamlines comparison at $Re = 7500$ and $Re = 10000$. The first row shows the CFD results; the second row shows the results obtained by the FFV-PINN model. From left to right: global streamlines, and detailed streamlines of the bottom-left corner, bottom-right corner, and top-left corner, respectively.

Fig. 8 presents the velocity profiles for u along vertical lines and v along horizontal lines, both passing through the geometric center of the cavity. Across the range of Re considered, the FFV-PINN method demonstrates consistency with established numerical solutions reported by Ghia (Ghia et al., 1982). Specifically, the extreme — both maximum and minimum values — of the velocity components predicted by the FFV-PINN exhibits close quantitative correspondence to

benchmark data.

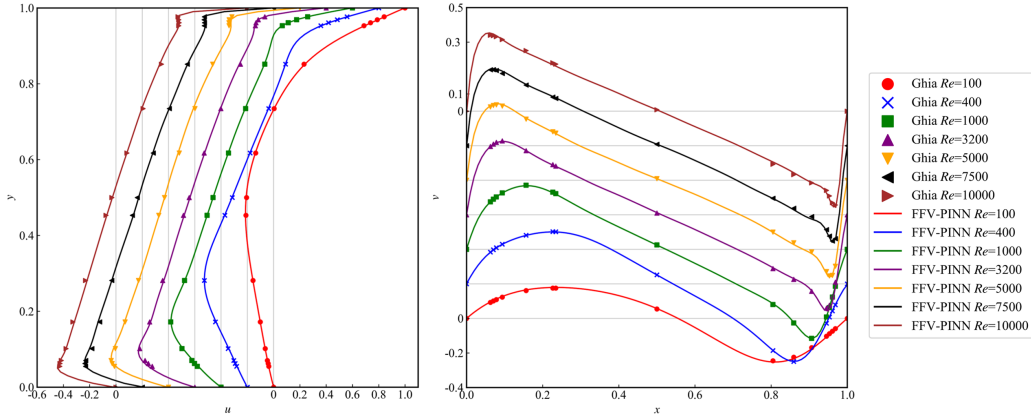


Figure 8: Comparison of the velocity profiles between the FFV-PINN and the numerical results from Ghia. Left: Comparison of u -velocity along vertical lines through the geometric center. Right: Comparison of profiles of v -velocity along horizontal lines through the geometric center.

Fig. 9 presents a detailed analysis of the evolution of vortex center positions, including primary vortex and secondary vortices, across multiple Re ($Re = 100, 400, 1000, 3200, 5000, 7500,$ and 10000). The FFV-PINN method exhibits remarkable accuracy in predicting the vortex centers of the primary vortex, BL1, and BR1, with their displacement across Re aligning closely with both CFD simulations and the benchmark data from Ghia. Discrepancies are noted for the TL1, BL2, and BR2 vortices, likely due to their relatively small magnitudes, which complicates the precise resolution of their positions. Despite these minor deviations, the overall consistency in vortex position underscores the effectiveness of the FFV-PINN method in capturing complex vortex structures across diverse flow conditions. Nonetheless, these discrepancies highlight potential avenues for further refinement, particularly in resolving fine-scale flow structures and enhancing the accuracy of secondary vortices. Addressing these aspects may further improve the model’s precision and extend its applicability to even more complex fluid dynamics problems.

Table 3 provides a quantitative evaluation of the model’s accuracy relative to ground truth CFD solutions (Chiu, 2018). These metrics are computed for the velocity components u , v , and the velocity magnitude V across a range of Re . In addition, the table details the training time and sample points used for each case. As expected, both MSE and relative L_2 error exhibit an increasing trend with Re , reflecting the greater challenge of accurately predicting increasingly

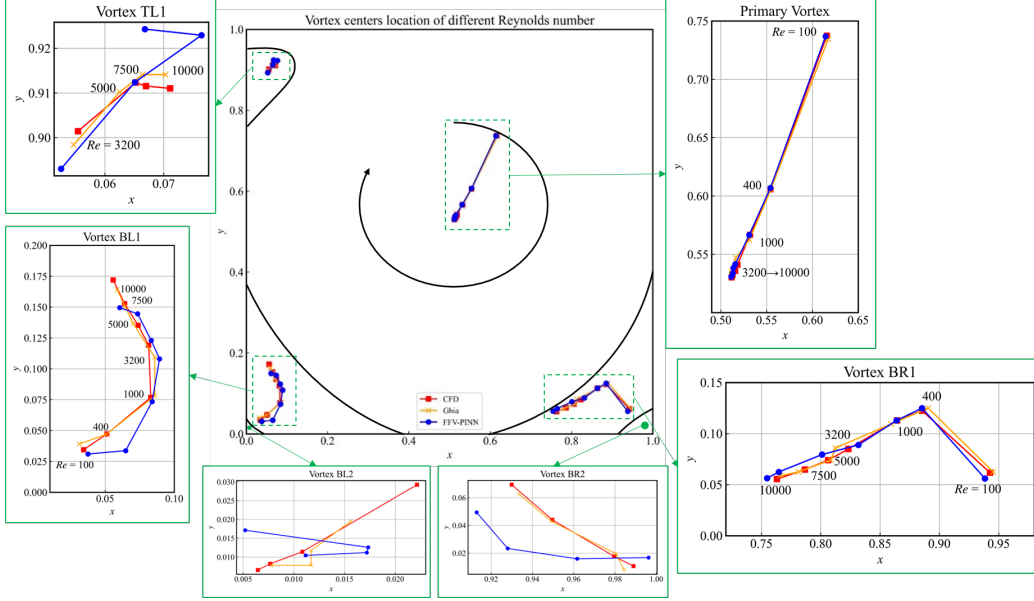


Figure 9: A comparative analysis of the vortex center locations across varying Re . The central plot displays the overall domain of the lid-driven cavity, with six enlarged subplots embedded within it. Each subplot focuses on a specific region of interest where secondary vortices are expected to form: the Top-Left corner (TL1), the Bottom-Left corner (BL1 and BL2), the Bottom-Right corner (BR1 and BR2), and the Primary Vortex core. Each subplot compares the vortex center locations obtained from CFD (red squares), the proposed FFV-PINN model (blue circles), and the Ghia (orange cross).

complex flow behavior at higher Re . Despite this trend, the model maintains an

Table 3: Quantitative evaluation of model accuracy for lid-driven cavity flow at various Re . The sample points indicate the product of grid points. For 2D steady cases, this corresponds to the product of the number of grid points in the x and y directions.

Re	MSE			Relative L_2 Error			Time (s)	Sample points
	u	v	V	u	v	V		
100	4.77e-05	1.99e-05	2.80e-05	3.51e-02	2.88e-02	2.12e-02	129	51×51
400	9.41e-06	7.22e-06	9.79e-06	1.49e-02	1.42e-02	1.12e-02	209	101×101
1000	8.95e-06	7.61e-06	1.48e-05	1.36e-02	1.40e-02	1.30e-02	180	128×128
3200	7.11e-05	6.28e-05	1.30e-04	3.78e-02	3.72e-02	3.69e-02	229	256×256
5000	7.60e-05	7.00e-05	1.36e-04	4.05e-02	4.05e-02	3.90e-02	237	256×256
7500	5.45e-05	4.51e-05	9.04e-05	3.44e-02	3.12e-02	3.13e-02	241	256×256
10000	4.45e-05	4.43e-05	8.06e-05	3.19e-02	3.17e-02	3.03e-02	680	256×256

excellent level of accuracy across the entire range of Re . At lower Re (e.g., Re

= 100), the model exhibits very small errors, with MSE of $V = 2.80\text{e-}05$ and relative L_2 error of $V = 2.12\text{e-}02$, which is indicative of its ability to accurately capture laminar flow dynamics. Even at higher Re (e.g., $Re = 10000$), where the flow becomes increasingly complex and turbulent, the model provides reasonably accurate predictions, with MSE of $V = 8.06\text{e-}05$ and relative L_2 error of $V = 3.03\text{e-}02$.

An increase in training time with Re is observed, which aligns with the greater computational demands required to resolve the finer flow details present at higher Re . This is also consistent with the increase in mesh resolution required for traditional CFD at higher Re to accurately capture the increasingly complex flow structures. However, despite these challenges, the FFV-PINN method converges rapidly to an accurate solution across all Re . Even at $Re=10000$, the required computation time is only about 10 minutes.

To further demonstrate the capabilities and robustness of the FFV-PINN framework, the 2D unsteady lid-driven cavity flow at $Re = 400$ and the 3D steady lid-driven cavity flow at $Re = 1000$ are investigated. The governing equations for the 2D unsteady lid-driven cavity are expressed by:

$$\frac{\partial u}{\partial x} + \frac{\partial v}{\partial y} = 0 \quad (38a)$$

$$\frac{\partial u}{\partial t} + \frac{\partial (uu)}{\partial x} + \frac{\partial (vu)}{\partial y} = \frac{1}{Re} \left(\frac{\partial^2 u}{\partial x^2} + \frac{\partial^2 u}{\partial y^2} \right) - \frac{\partial p}{\partial x} \quad (38b)$$

$$\frac{\partial v}{\partial t} + \frac{\partial (uv)}{\partial x} + \frac{\partial (vv)}{\partial y} = \frac{1}{Re} \left(\frac{\partial^2 v}{\partial x^2} + \frac{\partial^2 v}{\partial y^2} \right) - \frac{\partial p}{\partial y} \quad (38c)$$

Unlike the steady incompressible N-S equations, the unsteady form includes the temporal derivative term in the momentum equations, which is computed using AD.

Fig. 10 presents the contours of velocity magnitude V at several representative time instances for the 2D unsteady lid-driven cavity flow at $Re = 400$. The velocity fields predicted by the proposed FFV-PINN show excellent agreement with those obtained from high-fidelity CFD simulations (Chiu, 2018) across all time steps. As time progresses, the FFV-PINN accurately captures the formation and evolution of the primary vortex, a hallmark feature of unsteady lid-driven cavity flows. Moreover, the absolute error distributions indicate that the FFV-PINN maintains uniformly low prediction errors across the spatial domain. Crucially, these errors remain stable over time, showing no evidence of temporal accumulation. This demonstrates the model’s ability to preserve accuracy over long-duration unsteady simulations, which is essential for modeling time-dependent fluid dynamics.

Fig 11 illustrates the temporal evolution of the horizontal velocity component u at the geometric center of the cavity. The predictions from FFV-PINN closely

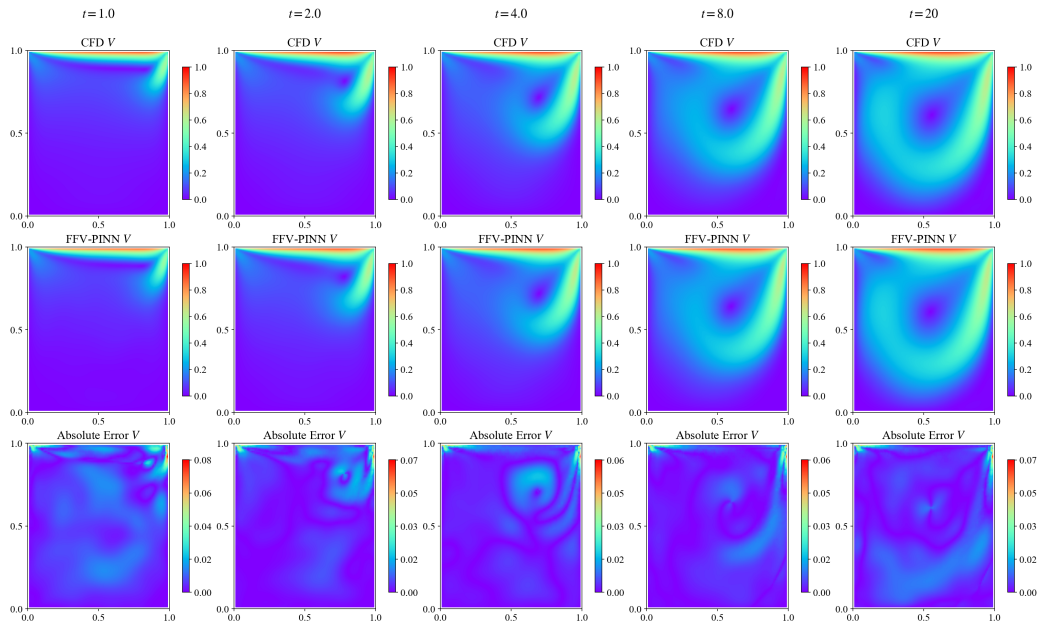


Figure 10: Comparison of the vertical magnitude (V) contours at different time instances ($t = 1.0, 2.0, 4.0, 8.0, 20.0$) for the 2D unsteady lid-driven cavity flow ($Re = 400$). The top row shows CFD results, the middle row shows FFV-PINN predictions, and the bottom row displays the absolute error between them.

match the CFD results (Chiu, 2018) over the entire simulation period, and both show excellent agreement with benchmark data from Kim et al. (Kim et al., 2002) and Dailey et al. (Dailey and Pletcher, 1996). This consistency validates the accuracy and reliability of the FFV-PINN framework in capturing transient flow dynamics.

The 3D lid-driven cavity problem is defined in a unit cubic domain $\Omega = [0, 1]^3$, where all six boundaries are solid walls, as illustrated in Fig. 12. The top lid, located at $y = 1$, moves uniformly in the x -direction with a constant velocity $u = 1$, while all other walls remain stationary and satisfy no-slip boundary conditions. The governing equations for this steady incompressible flow problem are given by:

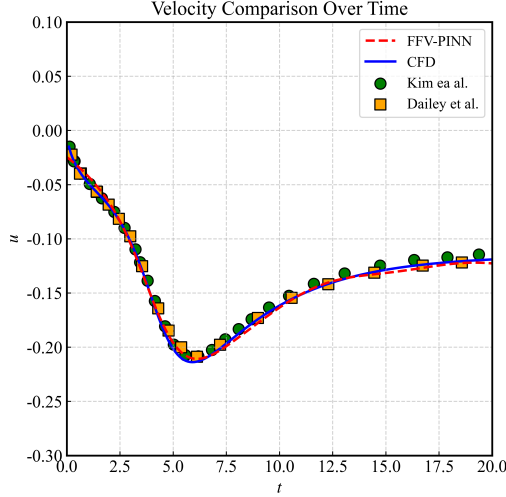


Figure 11: Temporal evolution of the horizontal velocity component u at the geometric center point $(0.5, 0.5)$ of the 2D cavity. The plot compares FFV-PINN predictions (red dashed line) with high-fidelity CFD results (blue solid line) and established benchmark data from Kim et al. (Kim et al., 2002) (green circles) and Dailey et al. (Dailey and Pletcher, 1996) (orange squares).

$$\frac{\partial u}{\partial x} + \frac{\partial v}{\partial y} + \frac{\partial w}{\partial z} = 0 \quad (39a)$$

$$\frac{\partial(uu)}{\partial x} + \frac{\partial(vu)}{\partial y} + \frac{\partial(wu)}{\partial z} = -\frac{\partial p}{\partial x} + \frac{1}{Re} \left(\frac{\partial^2 u}{\partial x^2} + \frac{\partial^2 u}{\partial y^2} + \frac{\partial^2 u}{\partial z^2} \right) \quad (39b)$$

$$\frac{\partial(uv)}{\partial x} + \frac{\partial(vv)}{\partial y} + \frac{\partial(wv)}{\partial z} = -\frac{\partial p}{\partial y} + \frac{1}{Re} \left(\frac{\partial^2 v}{\partial x^2} + \frac{\partial^2 v}{\partial y^2} + \frac{\partial^2 v}{\partial z^2} \right) \quad (39c)$$

$$\frac{\partial(uw)}{\partial x} + \frac{\partial(vw)}{\partial y} + \frac{\partial(ww)}{\partial z} = -\frac{\partial p}{\partial z} + \frac{1}{Re} \left(\frac{\partial^2 w}{\partial x^2} + \frac{\partial^2 w}{\partial y^2} + \frac{\partial^2 w}{\partial z^2} \right) \quad (39d)$$

Fig. 13 presents the contours of velocity magnitude V on the $z=0.5$ plane for the 3D lid-driven cavity flow at $Re = 1000$. The velocity fields predicted by the FFV-PINN show a high degree of consistency with CFD results (Chiu, 2018). This agreement suggests that the proposed approach is capable of maintaining reliable predictive performance in 3D scenarios, indicating its potential applicability to complex spatial problems. The pointwise absolute error distribution further supports this observation, showing uniformly low errors across the domain, with only a slight increase near the top-right corner.

Fig. 14 presents a comparison of centerline velocity profiles predicted by the

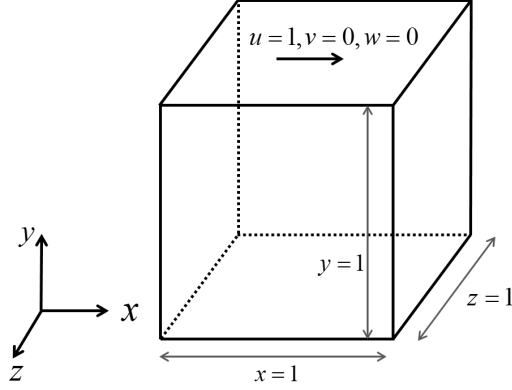


Figure 12: Geometry of the 3D lid-driven cavity

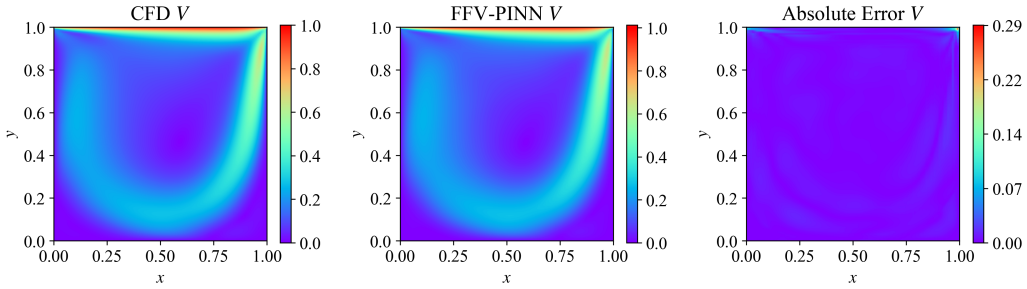


Figure 13: Comparison of the velocity magnitude V distributions on the $z = 0.5$ plane obtained from CFD simulations, the FFV-PINN model, and their corresponding pointwise absolute error

FFV-PINN with our in-house CFD results (Chiu, 2018) and reference benchmark data from literature (Ku et al., 1987). It is clearly evident from the figure that the predictions of the FFV-PINN show a high degree of consistency with those of Ku et al. (Ku et al., 1987) and the CFD for both the horizontal velocity component u and the vertical component v , highlighting the remarkable accuracy and robustness of the FFV-PINN model in capturing the complex flow dynamics.

Table 4 presents a quantitative evaluation of the FFV-PINN on two benchmark problems: the 2D unsteady and 3D steady lid-driven cavity flow. Evaluation metrics include the relative L_2 error and MSE for the velocity components u , v , and w , as well as the velocity magnitude V . Training time and sample points are also reported.

In terms of relative L_2 error, the FFV-PINN demonstrates good accuracy in both the 2D unsteady and 3D steady lid-driven cavity flow. Specifically, the relative L_2 error for the velocity magnitude V is 3.12×10^{-2} in the 2D unsteady case

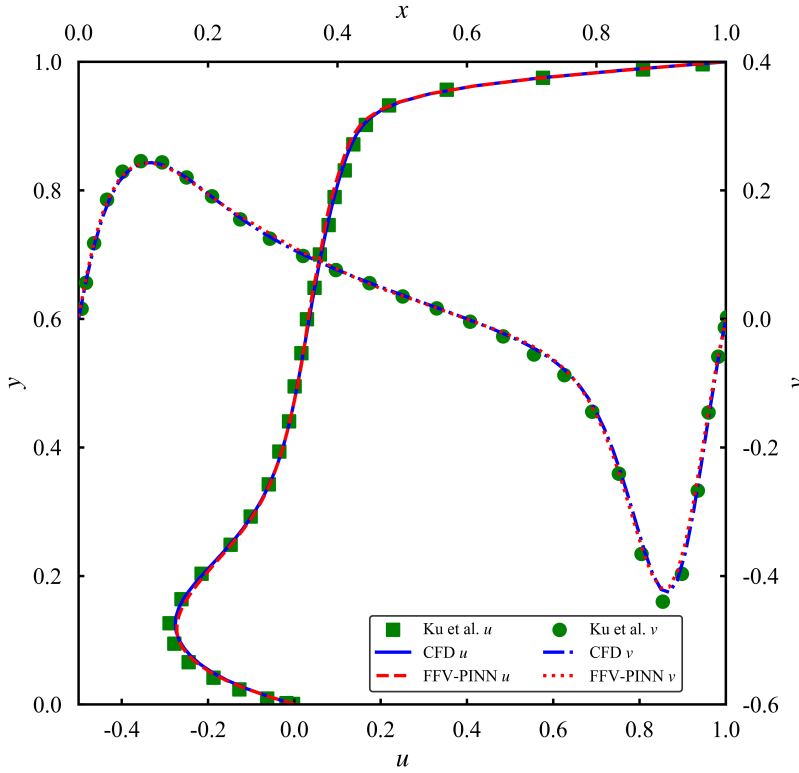


Figure 14: Comparison of velocity profiles along the centerlines of a 3D lid-driven cavity flow at $Re = 1000$. The horizontal velocity component u is plotted along the vertical centerline ($x = 0.5, z = 0.5$), with green squares representing the data from Ku et al. (Ku et al., 1987), the blue solid line indicating CFD results, and the red dashed line showing predictions by the FFV-PINN. The vertical velocity component v is plotted along the horizontal centerline ($y = 0.5, z = 0.5$), with green circles denoting the data from Ku et al. (Ku et al., 1987), the blue dash-dotted line indicating CFD results, and the red dash-dotted line representing FFV-PINN predictions.

and 5.09×10^{-2} in the 3D steady case. Although the error in the 3D case is slightly higher, this is expected given the increased complexity associated with higher spatial dimensions and the more intricate flow structures present in the 3D problem. From the perspective of MSE, a similar trend is observed. The MSE for the velocity magnitude V increases from 5.60×10^{-5} in the 2D case to 1.23×10^{-4} in the 3D case. Nevertheless, the error remains within an acceptable range, indicating that the model maintains accuracy despite the increased spatial complexity.

Furthermore, the training time remains relatively low for both cases, with the 3D case requiring 506s and the 2D case 564s, highlighting the computational

efficiency of the FFV-PINN. In summary, the proposed model not only achieves high numerical accuracy in both the 2D unsteady and the more complex 3D steady lid-driven cavity flow but also maintains consistently low training times across different scenarios. These results underscore the model’s strong generalization capability across various flow regimes, as well as its robustness and potential for a wide range of applications in flow prediction tasks spanning both steady and transient 2D and 3D flows.

Table 4: Quantitative evaluation of model accuracy for 2D unsteady and 3D steady lid-driven cavity flow. The sample points indicate the product of grid points. For 2D unsteady cases, this corresponds to the product of the number of grid points in time (t) and the spatial dimensions (x and y), while for 3D cases, it denotes the product of the grid points in the x , y , and z directions.

Case (Sample points)	Relative L_2 Error				MSE				Time
	u	v	w	V	u	v	w	V	
2D unsteady LDC ($200 \times 100 \times 100$)	3.74e-02	3.74e-02	-	3.12e-02	4.65e-05	3.39e-05	-	5.60e-05	564s
3D steady LDC ($128 \times 128 \times 128$)	5.52e-02	5.94e-02	2.25e-01	5.09e-02	8.78e-05	6.49e-05	1.60e-05	1.23e-04	506s

3.2. Backward-facing step flow

The backward-facing step flow serves as another critical benchmark for evaluating the capability of numerical methods to resolve separated flows. In this study, we consider flow within a 20×1 unit channel, with a fully developed parabolic velocity profile imposed at the inlet. The problem is schematically illustrated in Fig. 15. As the fluid flows over the backward-facing step, the abrupt expansion of the channel cross-section induces flow separation at the step corner (i.e., the point where the expansion begins).

At a steady state, a primary recirculation zone immediately forms at the downstream of the step. Its extension is characterized by the location x_1 . With increasing Re , flow bifurcation occurs, leading to the development of a secondary vortex structure along the upper channel wall between x_2 and x_3 . Despite having different boundary conditions, the backward-facing step flow shares the same physical laws as the lid-driven cavity flow, both being governed by the steady-state, 2D, incompressible N-S equations, as detailed in Eq.3.

Table 5 presents comparative results of key flow characteristics in the backward-facing step problem, specifically focusing on the detachment and reattachment points (x_1 , x_2 , and x_3) obtained from different PINN models. The predicted x_1 positions from our FFV-PINN show remarkable consistency with CFD (Chiu,

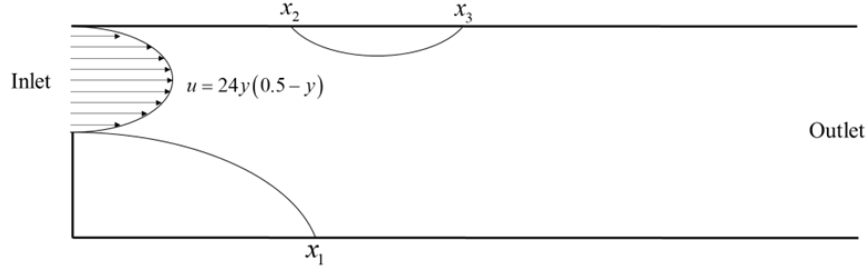


Figure 15: Schematic representation of the backward-facing step flow problem. A fully developed parabolic velocity profile, defined by $u = 24y(0.5 - y)$, is imposed at the inlet. Key locations of interest are denoted as x_1 , x_2 , and x_3 , which typically represent the detachment and reattachment points.

2018) results at $Re = 200$ and $Re = 400$. Furthermore, the FFV-PINN’s predicted x_2 and x_3 values at $Re = 400$ also fall within the range reported by other CFD methods, further demonstrating the accuracy of our model in capturing flow separation and reattachment dynamics.

Table 5: Comparison of detachment and reattachment points from PINN-based predictions and benchmark solutions for the backward-facing step problem

References	200		400	
	x_1	x_1	x_2	x_3
CFD, Barton (Barton, 1995)	2.565	4.255	4.045	5.11
CFD, Barber et al.(Barber and Fonty, 2001)	2.635	4.265	4.065	5.07
CFD, Erturk (Erturk, 2008)	2.491	4.119	3.866	5.019
CFD, Chiu (Chiu, 2018)	2.608	4.305	4.091	5.122
CAN-PINN (Chiu et al., 2022)	2.604	4.292	4.120	5.161
LSFD-PINN (Xiao et al., 2024)	2.614	4.243	4.113	5.071
RBFdq-PINN-II (Xiao et al., 2023)	2.632	4.212	4.069	5.130
Ours	2.609	4.307	4.145	5.089

Fig. 16 presents the contours of the backward-facing step flow at $Re = 800$. In this case, the λ_{de} , λ_{bc} , λ_{rc} , and α are set to 10.0, 10.0, 1.0, and 0.95, respectively. The FFV-PINN demonstrates a high level of accuracy in capturing both the u -velocity and v -velocity profile. The absolute error plots highlight the low discrepancies between FFV-PINN predictions and the CFD benchmarks, further validating the model’s ability to capture overall flow behavior accurately.

Fig. 17 presents streamline visualizations illustrating the flow patterns associated with the backward-facing step problem at $Re = 800$. The results obtained

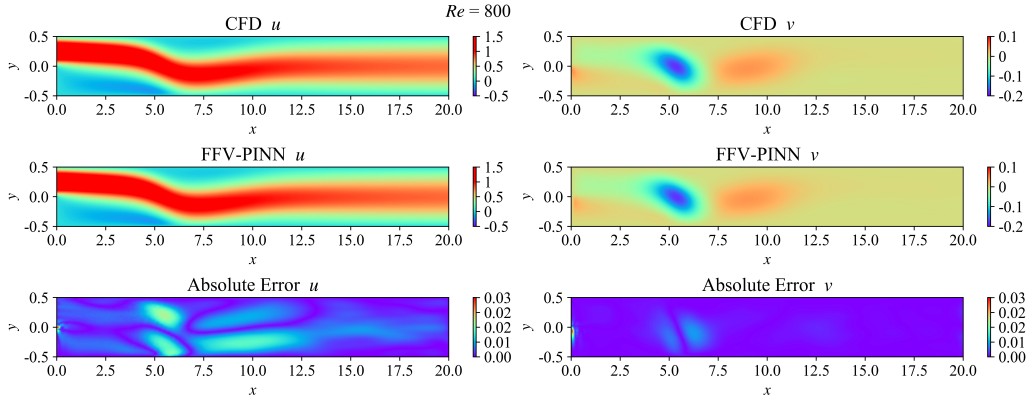


Figure 16: Velocity contour and absolute point-wise error distribution for the backward-facing step flow at $Re = 800$. From top to bottom, the figures are as follows: u -velocity (left) and v -velocity (right) contours from CFD; u -velocity and v -velocity contours from the FFV-PINN; absolute point-wise error in u -velocity and v -velocity.

from the FFV-PINN exhibit a strong qualitative agreement with the predictions generated by CFD simulations. Significantly, the FFV-PINN model accurately replicates the formation of the recirculation zone immediately behind the step, as well as the emergence of a secondary eddy in the upper mid-region of the channel. These flow structures are fundamental features of backward-facing step flow, highlighting the model’s capability to capture the essential dynamics of separated flows with a high degree of fidelity.

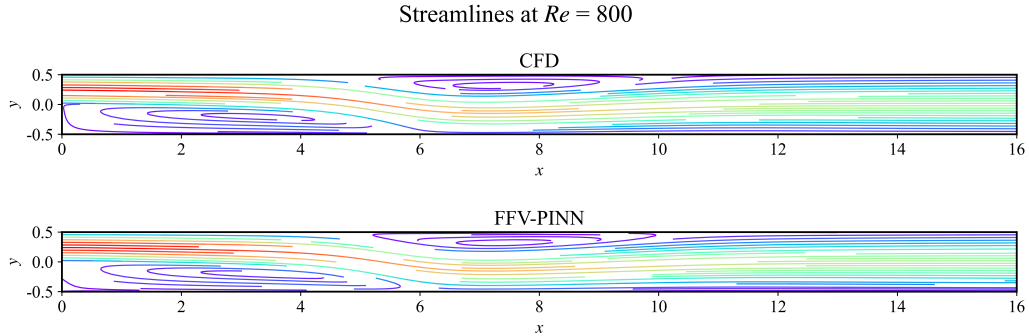


Figure 17: Streamlines for the backward-facing step flow at $Re = 800$. The top panel presents the streamlines obtained from the CFD solution of Chiu (Chiu, 2018), while the bottom panel shows the streamlines from the FFV-PINN model. The color of the streamlines represents the velocity magnitude V .

Fig 18 displays a systematic comparison of the streamwise velocity u profiles

at $Re = 800$, evaluated at three critical downstream positions ($x = 3$, $x = 7$, and $x = 15$). At $x = 3$, immediately downstream of the step, the u -velocity distribution exhibits a steep shear layer near the bottom wall, marking the formation of the primary recirculation vortex. This region is characterized by flow reversal and serves as the dominant separation zone. Further downstream at $x = 7$, a secondary

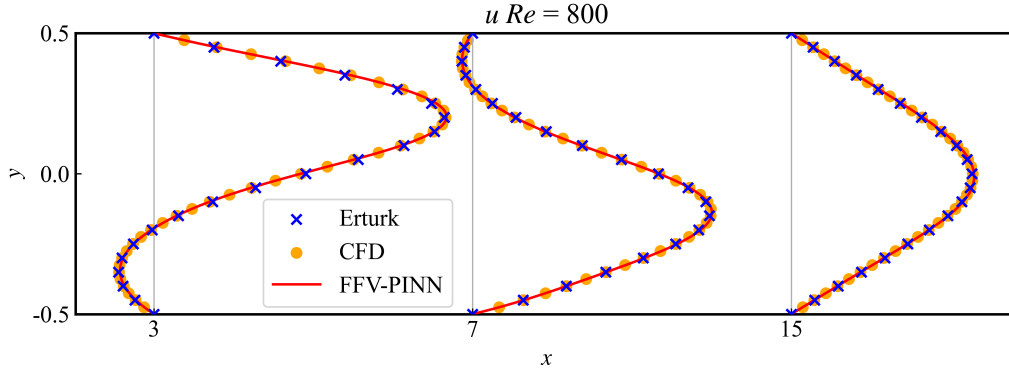


Figure 18: Comparison of u -velocity profiles at $Re = 800$ for the backward-facing step flow. Profiles are shown at various x -locations ($x = 3$, $x = 7$, and $x = 15$) along the channel, comparing results from the FFV-PINN (red line), CFD solution of Chiu (Chiu, 2018)(orange circles), and benchmark data from Erturk (Erturk, 2008) (blue crosses).

vortex emerges near the upper wall, as evidenced by localized velocity inflection points. At $x = 15$, the flow achieves full redevelopment. The strong agreement observed across all x -locations between the FFV-PINN results and both the CFD solution of Chiu (Chiu, 2018) and the benchmark data from Erturk (Erturk, 2008) highlights the model’s ability to accurately predict the velocity distribution within the channel. This consistency further validates the effectiveness of the FFV-PINN in resolving key flow characteristics, including shear layer development and recirculation dynamics, across different regions of the flow domain.

Table 6 presents a quantitative evaluation of the FFV-PINN model accuracy for backward-facing step flow at various Re by utilizing CFD solutions as ground truth (Chiu, 2018). The results indicate that the model maintains very low errors across all investigated Re . Specifically, for $Re = 100$, the relative L_2 error for the velocity components u and v are $1.63e-03$ and $1.12e-02$ respectively. Even at $Re = 800$, the errors remain small, with $8.41e-03$ for u and $3.48e-02$ for v . The training time remains constant at 171 seconds for all cases, indicating that the model’s efficiency does not degrade with increasing Re . Additionally, the error values show no significant fluctuations as Re increases, demonstrating that the model maintains stable performance across different flow conditions.

Table 6: Quantitative evaluation of model accuracy for backward-facing step flow at various Re

Re	MSE			Relative L_2 Error			Time (s)	Sample points
	u	v	V	u	v	V		
100	8.67e-07	1.02e-07	8.72e-07	1.63e-03	1.12e-02	1.64e-03	171	801×41
200	2.51e-06	1.64e-07	2.32e-06	2.72e-03	1.61e-02	2.61e-03	171	801×41
400	5.66e-06	3.78e-07	5.48e-06	3.93e-03	2.55e-02	3.87e-03	171	801×41
600	9.41e-06	3.37e-07	9.32e-06	4.89e-03	2.08e-02	4.86e-03	171	801×41
800	2.97e-05	1.25e-06	2.95e-05	8.41e-03	3.48e-02	8.38e-03	171	801×41

3.3. Natural convection in a unit square

Natural convection is a vital, multi-physics phenomenon in both the natural sciences and engineering fields, involving the interplay between fluid flow and heat transfer. Addressing such problems requires solving a multi-physics scenario with thermal-fluid interactions as per the N-S equations and energy equation. For the current problem, the computational domain is a unit square, as shown in Fig 19. The vertical boundaries are maintained at distinct temperatures: the left wall is set to $T(x = 0, y) = 1$ while the right wall remains at $T(x = 1, y) = 0$. The horizontal surfaces are characterized by zero thermal flux conditions ($\frac{\partial T}{\partial n} = 0$), creating thermally adiabatic interfaces that prevent heat exchange with the external environment. The governing equations for this system are expressed by:

$$\frac{\partial u}{\partial x} + \frac{\partial v}{\partial y} = 0 \quad (40a)$$

$$u \frac{\partial u}{\partial x} + v \frac{\partial u}{\partial y} = \sqrt{\frac{Pr}{Ra}} \left(\frac{\partial^2 u}{\partial x^2} + \frac{\partial^2 u}{\partial y^2} \right) - \frac{\partial p}{\partial x} \quad (40b)$$

$$u \frac{\partial v}{\partial x} + v \frac{\partial v}{\partial y} = \sqrt{\frac{Pr}{Ra}} \left(\frac{\partial^2 v}{\partial x^2} + \frac{\partial^2 v}{\partial y^2} \right) - \frac{\partial p}{\partial y} + T \quad (40c)$$

$$u \frac{\partial T}{\partial x} + v \frac{\partial T}{\partial y} = \frac{1}{\sqrt{PrRa}} \left(\frac{\partial^2 T}{\partial x^2} + \frac{\partial^2 T}{\partial y^2} \right) \quad (40d)$$

where Pr denotes the Prandtl number representing the ratio of momentum diffusivity to thermal diffusivity and is fixed to 0.71. Ra represents the Rayleigh number describing the relationship between buoyancy and viscosity of the fluid. An increase in Ra signifies that the buoyancy forces, which drive the flow due to temperature differences, become significantly stronger relative to the viscous forces that resist motion. This transition can lead to a variety of nonlinear effects that can be quite complex and multifaceted.

Fig 20 provides contours for the evaluation of FFV-PINN in simulating natural convection phenomena at a high Ra ($Ra = 10^8$). The λ_{de} , λ_{bc} , λ_{rc} , and α are set to

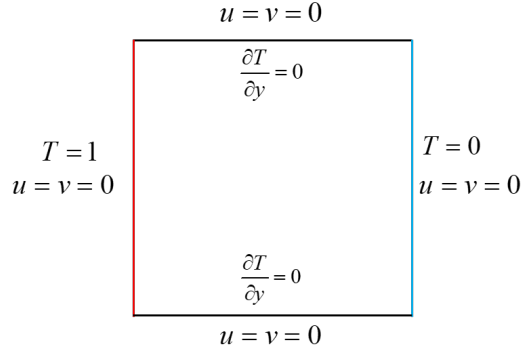


Figure 19: Schematic of the natural convection problem in a square cavity. The left and right walls are maintained at constant temperatures $T = 1$ and $T = 0$, respectively, while the top and bottom walls are adiabatic with $\frac{\partial T}{\partial y} = 0$. No-slip boundary conditions ($u = v = 0$) are imposed on all four walls.

1.0, 1.0, 1.0, and 0.84, respectively. The FFV-PINN results demonstrate excellent agreement with CFD benchmarks (Chiu, 2018) in reconstructing the temperature distribution and velocity field. Notably, the FFV-PINN model effectively captures thin thermal boundary layers, which are critical for accurately simulating heat transfer in buoyancy-driven flows. In addition, the low error magnitudes also confirm the model’s capacity to solve problems involving coupled flow and heat transfer.

Table 7 presents a comparison of the average Nusselt number (\overline{Nu}) and the maximum vertical velocity (v_{\max}) obtained from the proposed FFV-PINN model against established reference values (Kalita et al., 2001) and CFD results (Chiu, 2018). The FFV-PINN model exhibits excellent agreement with benchmark data for \overline{Nu} , t. Specifically, at $Ra = 10^6$, FFV-PINN yields an \overline{Nu} of 8.695, closely approximating the reference value of 8.829 and the CFD result of 8.785. Furthermore, by employing a refined 202×202 grid at higher Ra (5×10^7 and 10^8), the model produces predictions of $\overline{Nu} = 24.87$ and $\overline{Nu} = 29.50$ respectively, which are very close to the CFD results of $\overline{Nu} = 25.27$ and $\overline{Nu} = 30.34$. These results underscore the accuracy of our FFV-PINN model in capturing the complex physics of natural convection, even under challenging high Ra conditions.

For the v_{\max} along the horizontal midline, it is noted that due to the fact that the non-dimensional equations we derived are different from (Kalita et al., 2001; Chiu, 2018), the scaling factor of \sqrt{RaPr} is employed for comparisons. At $Ra = 10^7$, using a 75×75 grid, the FFV-PINN model slightly underestimates v_{\max} compared to the CFD results. However, upon refining the grid resolution to 202×202 , the FFV-PINN predictions become nearly identical to those from

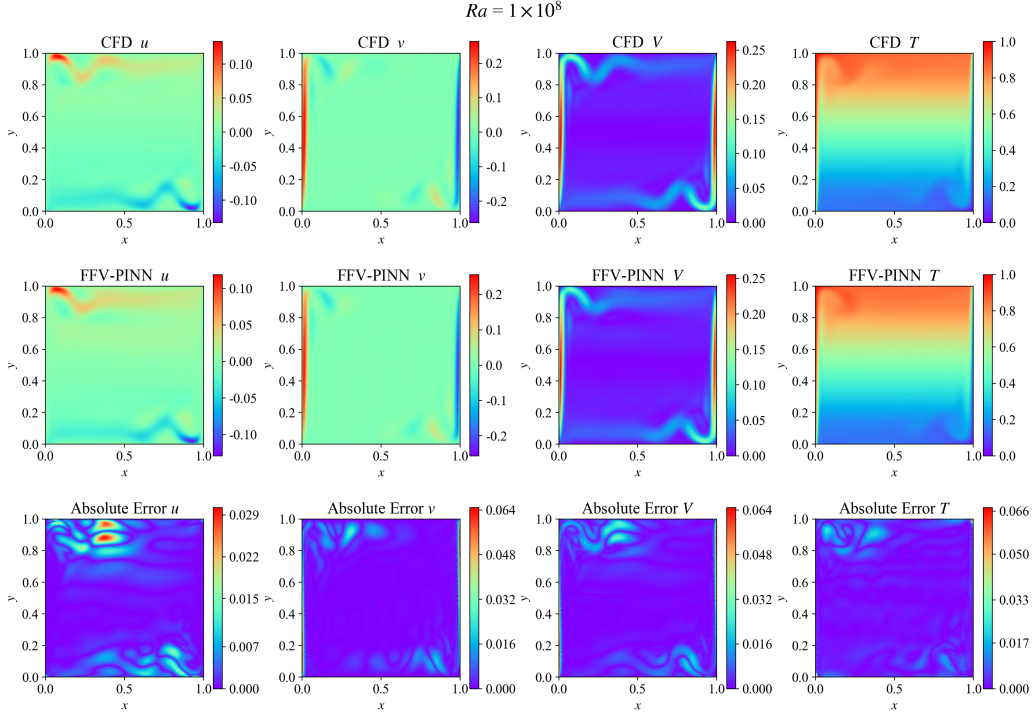


Figure 20: The velocity and temperature comparison for natural convection in a square cavity at $Ra = 10^8$. The figure presents a comparative analysis of u -velocity, v -velocity, velocity magnitude V , and temperature T contours obtained from CFD solution of Chiu(Chiu, 2018) (top row), the FFV-PINN model (middle row), and the absolute error between them (bottom row).

CFD. At higher Ra (5×10^7 and 10^8), the model continues to underestimate v_{max} relative to the CFD outcomes. Despite these discrepancies, it is important to note that the magnitude of the differences is relatively small, and the errors remain within acceptable limits. In summary, these comparisons indicate that our method produces results that are very close to established benchmarks. The observed differences between numerical methods may be attributed to grid resolution and increased nonlinearity at higher Ra . A more detailed comparison is provided in Appendix C.

Table 8 presents a quantitative evaluation of the FFV-PINN model's accuracy in simulating natural convection across a range of Ra ($Ra = 10^6$ to 10^8) by utilizing CFD solutions as ground truth(Chiu, 2018). The model's performance is assessed using MSE and relative L_2 error for the u -velocity, v -velocity, and temperature (T) fields. Training time and sample points are also provided. The

Table 7: Comparison of average Nusselt number (\overline{Nu}) and maximum vertical velocity (v_{max}) at various Ra for different methods.

References (Mesh/Sample points)	Parameters	Ra			
		10^6	10^7	5×10^7	10^8
CFD, Kalita et al. (81×81)(Kalita et al., 2001)	\overline{Nu}	8.829	16.52	–	–
	v_{max}	221.66	696.2	–	–
CFD, Chiu (75×75)(Chiu, 2018)	\overline{Nu}	8.785	16.46	–	–
	v_{max}	215.80	681.73	–	–
CFD, Chiu (202×202) (Chiu, 2018)	\overline{Nu}	–	16.50	25.27	30.34
	v_{max}	–	695.22	1543.92	2202.26
Ours (75×75)	\overline{Nu}	8.695	16.31	–	–
	v_{max}	216.42	674.78	–	–
Ours (202×202)	\overline{Nu}	–	16.34	24.87	29.50
	v_{max}	–	696.33	1443.62	2129.92

FFV-PINN model exhibits excellent performance across the Ra considered. While both the MSE and relative L_2 error metrics generally increase with increasing Ra , the magnitude of these errors remains remarkably low, even at the highest Ra value of 10^8 . This indicates the model’s ability to accurately capture the complex interplay of buoyancy and diffusion that characterizes natural convection, even as the flow transitions towards a more nonlinear regime. The training time remains consistently low across all Ra ranges, varying between 150s and 231s, thus confirming the efficiency of the FFV-PINN model. Last, it is worth noting that, to the best of the authors’ knowledge, this work represents the first successful application of a PINN-based method to natural convection problems at $Ra = 10^8$. This achievement underscores the capability of the FFV-PINN model to address highly complex flow regimes, marking a significant advancement in the application of machine learning techniques to challenging fluid dynamics problems.

4. Conclusion

In this study, we present the FFV-PINN, an innovative framework that synergistically integrates a simplified FVM with the residual correction loss term. This framework effectively mitigates two primary shortcomings commonly associated with vanilla PINNs: the inadequate enforcement of physical constraints in the loss function due to the omission of information from neighboring points, and the challenges related to poor convergence during the training process.

Table 8: Quantitative evaluation of model accuracy for natural convection at various Ra

Ra	MSE			Relative L_2 Error			Time (s)	Sample points
	u	v	T	u	v	T		
10^6	1.42e-06	2.01e-06	6.25e-06	2.52e-02	2.09e-02	4.51e-03	164	50×50
10^6	1.12e-06	1.44e-06	4.95e-06	2.24e-02	1.76e-02	4.01e-03	154	75×75
10^7	4.30e-06	4.50e-06	6.34e-06	6.90e-02	4.05e-02	6.03e-03	150	75×75
10^7	3.47e-06	1.94e-06	9.84e-06	6.18e-02	2.62e-02	5.65e-03	225	202×202
5×10^7	3.55e-06	3.45e-06	1.38e-05	8.69e-02	4.19e-02	6.67e-03	230	202×202
10^8	1.56e-05	1.09e-05	1.37e-05	2.12e-01	8.07e-02	6.65e-03	231	202×202

Traditional FVM is well-known for its inherent mechanisms that enforce conservation laws, which often leads to solutions that are not only stable but also reliable. However, selecting an appropriate discretization scheme for the convection term remains non-trivial, necessitating a comprehensive understanding of the underlying physical phenomena as well as the strengths and limitations of the available numerical methods. In FFV-PINN, we simplify this process by directly leveraging neural network outputs on control surfaces, strengthening the enforcement of physical constraints while reducing the complexity of discretization. Moreover, the residual correction loss plays a crucial role in improving both stability and convergence, making the training process more robust. By guiding the training direction of the neural network, this term ensures that updates are executed in a manner that aligns with the fulfillment of physical constraints. As a result, the FFV-PINN framework mitigates the issues of poor convergence and fosters a highly efficient training environment.

To validate the effectiveness of the proposed FFV-PINN framework, we conducted a comprehensive evaluation by applying it to a series of challenging benchmark problems, including 2D steady and unsteady lid-driven cavity flows, 3D steady lid-driven cavity flow, backward-facing step flow, and natural convection. The results, when compared with existing literature, demonstrate that FFV-PINN significantly enhances both accuracy and computational efficiency. This improvement is particularly evident in the framework’s ability to achieve higher solution precision while requiring substantially less training time. Without incorporating additional data, previous studies on PINNs have only been able to solve the lid-driven cavity flow problem up to $Re = 5000$, while requiring substantial computational resources and time. In contrast, our FFV-PINN successfully extends the solution to $Re = 10000$, a highly non-linearity regime that has not been achieved by other PINN methods, while reducing training time significantly. This achievement underscores the capability of FFV-PINN to address complex fluid dynamics scenarios. Furthermore, FFV-PINN also demonstrates high accuracy and compu-

tational efficiency when solving 2D unsteady and 3D flow problems, underscoring the model’s capability and robustness.

Despite the promising results achieved with the FFV-PINN, it is important to acknowledge that the framework still has certain limitations. Specifically, for the lid-driven cavity flow at $Re = 10000$, the FFV-PINN fails to effectively capture the expected third small-scale vortex structure in the lower-left corner of the cavity. This limitation underscores the necessity for further advances in capturing small-scale phenomena, which are critical for accurately representing turbulent flow dynamics. Future research will focus on addressing this challenge by exploring strategies such as assigning greater weight to small-scale solutions during training. Additionally, we will consider integrating multi-grid techniques to enable adaptive refinement of the model’s grid or resolution in regions where small-scale phenomena are prominent.

Beyond these directions, another promising avenue lies in extending the FFV-PINN framework to incorporate higher-order FVM. Such extensions would involve reformulating the flux at cell interfaces and the discretization of diffusion terms using a higher-order interpolation scheme. While this would introduce additional computational complexity, it is expected to improve solution accuracy and better capture fine-scale features, particularly in high Re number. We consider this a valuable direction for future work, whereby one might opt for specific schemes to achieve the highest accuracy within acceptable computational resource limits, as is common in traditional scientific computing.

Acknowledgment

Chang Wei and Yuchen Fan would like to acknowledge support from the China Scholarship Council for the scholarship to conduct research at Agency for Science, Technology and Research (A*STAR).

This research is partially supported by the National Research Foundation, Singapore, and Civil Aviation Authority Singapore under the Aviation Transformation Programme - ”ATM-Met Integration of Convective Weather Forecast and Impact Forecast Solutions Supporting Singapore Air Traffic Operations [Award No. ATP2.0_ATM-MET_I2R], and the Singapore Ministry of Health’s National Medical Research Council under its National Epidemic Preparedness and Response R&D Funding Initiative (MOH-001041) Programme for Research in Epidemic Preparedness and REsponse (PREPARE) - ”Development of Risk Assessment Model for Infectious Respiratory Diseases Considering Human Mobility [Award No. PREPARE-CS1-2022-004].

Appendix A.

When employing the simplified FVM for the momentum equation, the coefficients and source term of Eq. 16 are as follows:

$$a_E = a_W = a_N = a_S = -\frac{1}{Re} \quad (\text{A.1a})$$

$$a_e = u_e \Delta y \quad (\text{A.1b})$$

$$a_w = -u_w \Delta y \quad (\text{A.1c})$$

$$a_n = v_n \Delta x \quad (\text{A.1d})$$

$$a_s = -v_s \Delta x \quad (\text{A.1e})$$

$$a_P = \frac{4}{Re} \quad (\text{A.1f})$$

$$b = \begin{cases} \frac{(p_E - p_W) \Delta y}{2} & \text{if } \phi = u \\ \frac{(p_N - p_S) \Delta x}{2} & \text{if } \phi = v \end{cases} \quad (\text{A.1g})$$

Appendix B.

- *CD Scheme*

The spatial derivative $\frac{\partial \phi}{\partial x}$ can be expressed as follows:

$$\frac{\partial \phi}{\partial x} = \frac{\phi_E - \phi_W}{2h} = \frac{\phi(x+h) - \phi(x-h)}{2h} \quad (\text{B.1})$$

Subsequently, the Fourier transform is applied to Eq. B.1.

$$2ikh \hat{\phi}(k) = e^{ikh} \hat{\phi}(k) - e^{-ikh} \hat{\phi}(k) \quad (\text{B.2})$$

Rearranging the above equation yields:

$$2ikh = e^{ikh} - e^{-ikh} \quad (\text{B.3})$$

By defining effective wavenumber $k' \cong k$, and multiplying both sides of the above equation by $-i$, we obtain

$$k' h = \frac{-i}{2} (e^{ikh} - e^{-ikh}) \quad (\text{B.4})$$

The real and imaginary parts of Eq. B.4 can then be expressed as:

$$\Re(k' h) = \Re \left[\frac{-i}{2} (e^{ikh} - e^{-ikh}) \right] = \sin(kh) \quad (\text{B.5a})$$

$$\Im(k' h) = \Im \left[\frac{-i}{2} (e^{ikh} - e^{-ikh}) \right] = 0 \quad (\text{B.5b})$$

- **FOU Scheme**

The spatial derivative $\frac{\partial\phi}{\partial x}$ can be expressed as:

$$\frac{\partial\phi}{\partial x} = \frac{\phi_e - \phi_w}{h} = \frac{\phi(x) - \phi(x-h)}{h} \quad (\text{B.6})$$

Subsequently, the Fourier transform is applied to Eq. B.6.

$$ikh\hat{\phi}(k) = \hat{\phi}(k) - e^{-ikh}\hat{\phi}(k) \quad (\text{B.7})$$

Rearranging the above equation yields:

$$ikh = 1 - e^{-ikh} \quad (\text{B.8})$$

By defining effective wavenumber $k' \cong k$, and multiplying both sides of the above equation by $-i$, we obtain

$$k'h = -i(1 - e^{-ikh}) \quad (\text{B.9})$$

The real and imaginary parts of Eq. B.9 can then be expressed as:

$$\Re(k'h) = \Re[-i(1 - e^{-ikh})] = \sin(kh) \quad (\text{B.10a})$$

$$\Im(k'h) = \Im[-i(1 - e^{-ikh})] = \cos(kh) - 1 \quad (\text{B.10b})$$

- **SOU Scheme**

The spatial derivative $\frac{\partial\phi}{\partial x}$ can be expressed as follows:

$$\frac{\partial\phi}{\partial x} = \frac{\phi_e - \phi_w}{h} = \frac{3\phi(x) - 4\phi(x-h) + \phi(x-2h)}{2h} \quad (\text{B.11})$$

Subsequently, the Fourier transform is applied to Eq. B.11.

$$2ikh\hat{\phi}(k) = (3 - 4e^{-ikh} + e^{-i2kh})\hat{\phi}(k) \quad (\text{B.12})$$

Rearranging the above equation yields:

$$2ikh = (3 - 4e^{-ikh} + e^{-i2kh}) \quad (\text{B.13})$$

By defining effective wavenumber $k' \cong k$, and multiplying both sides of the above equation by $-i$, we obtain

$$k'h = \frac{-i}{2}(3 - 4e^{-ikh} + e^{-i2kh}) \quad (\text{B.14})$$

The real and imaginary parts of Eq. B.14 can then be expressed as:

$$\Re(k'h) = \frac{1}{2}(4\sin(kh) - \sin(2kh)) \quad (\text{B.15a})$$

$$\Im(k'h) = \frac{-1}{2}(3 - 4\cos(kh) + \cos(2kh)) \quad (\text{B.15b})$$

Appendix C.

Table C.9: Comparison of numerical results at different Rayleigh numbers (Ra). Shown are the maximum horizontal velocity (u_{max}) with its location, maximum vertical velocity (v_{max}) with its location, and average Nusselt number (\overline{Nu}).

Method (Mesh/Sample points)	$Ra = 10^6$			$Ra = 10^7$			$Ra = 5 \times 10^7$			$Ra = 10^8$		
	u_{max}	v_{max}	\overline{Nu}	u_{max}	v_{max}	\overline{Nu}	u_{max}	v_{max}	\overline{Nu}	u_{max}	v_{max}	\overline{Nu}
CFD, Kalita et al. (81×81)(Kalita et al., 2001)	65.332 (0.850)	221.658 (0.038)	8.829	155.82 (0.863)	696.238 (0.025)	16.517	-	-	-	-	-	-
CFD, Chiu (75×75)(Chiu, 2018)	64.883 (0.847)	215.801 (0.034)	8.785	148.4308 (0.873)	681.7296 (0.020)	16.456	-	-	-	-	-	-
CFD, Chiu (202×202)(Chiu, 2018)	-	-	-	148.51 (0.882)	695.224 (0.025)	16.501	287.326 (0.938)	1543.921 (0.012)	25.277	333.533 (0.932)	2202.258 (0.012)	30.341
Ours (75×75)	64.885 (0.848)	216.423 (0.040)	8.695	133.506 (0.889)	674.779 (0.020)	16.312	-	-	-	-	-	-
Ours (202×202)	-	-	-	134.611 (0.879)	696.334 (0.020)	16.342	257.201 (0.939)	1443.615 (0.010)	24.872	303.094 (0.919)	2129.916 (0.010)	29.504

References

- Baez, A., Zhang, W., Ma, Z., Das, S., Nguyen, L.M., Daniel, L., 2024. Guaranteeing conservation laws with projection in physics-informed neural networks. arXiv preprint arXiv:2410.17445 .
- Barber, R., Fonty, A., 2001. Numerical simulation of confined laminar flow over a backward-facing step using a novel viscous-splitting vortex algorithm. *WIT Transactions on Modelling and Simulation* 30.
- Barton, I., 1995. A numerical study of flow over a confined backward-facing step. *International journal for numerical methods in fluids* 21, 653–665.
- Cai, S., Mao, Z., Wang, Z., Yin, M., Karniadakis, G.E., 2021. Physics-informed neural networks (pinns) for fluid mechanics: A review. *Acta Mechanica Sinica* 37, 1727–1738.
- Cao, W., Zhang, W., 2023. Tsonn: Time-stepping-oriented neural network for solving partial differential equations. arXiv preprint arXiv:2310.16491 .
- Cen, J., Zou, Q., 2024. Deep finite volume method for partial differential equations. *Journal of Computational Physics* 517, 113307.
- Chiu, P.H., 2018. An improved divergence-free-condition compensated method for solving incompressible flows on collocated grids. *Computers & Fluids* 162, 39–54.
- Chiu, P.H., Wong, J.C., Ooi, C., Dao, M.H., Ong, Y.S., 2022. Can-pinn: A fast physics-informed neural network based on coupled-automatic-numerical differentiation method. *Computer Methods in Applied Mechanics and Engineering* 395, 114909.
- Cuomo, S., Di Cola, V.S., Giampaolo, F., Rozza, G., Raissi, M., Piccialli, F., 2022. Scientific machine learning through physics-informed neural networks: Where we are and what’s next. *Journal of Scientific Computing* 92, 88.
- Dailey, L.D., Pletcher, R.H., 1996. Evaluation of multigrid acceleration for pre-conditioned time-accurate navier-stokes algorithms. *Computers & fluids* 25, 791–811.
- Darwish, F.M.L.M.M., 2016. The finite volume method in computational fluid dynamics.

- Dutta, S., Innan, N., Yahia, S.B., Shafique, M., 2024. Aq-pinns: Attention-enhanced quantum physics-informed neural networks for carbon-efficient climate modeling. arXiv preprint arXiv:2409.01626 .
- Erturk, E., 2008. Numerical solutions of 2-d steady incompressible flow over a backward-facing step, part i: High reynolds number solutions. *Computers & Fluids* 37, 633–655.
- Fabiani, G., Bolt, E., Siettos, C., Yannacopoulos, A.N., 2024. Stability analysis of physics-informed neural networks for stiff linear differential equations. arXiv preprint arXiv:2408.15393 .
- Finn, C., Abbeel, P., Levine, S., 2017. Model-agnostic meta-learning for fast adaptation of deep networks, in: *International conference on machine learning*, PMLR. pp. 1126–1135.
- Ghia, U., Ghia, K.N., Shin, C., 1982. High-re solutions for incompressible flow using the navier-stokes equations and a multigrid method. *Journal of computational physics* 48, 387–411.
- Gurieva, J., Vasiliev, E., Smirnov, L., 2022. Application of conservation laws to the learning of physics-informed neural networks. *Procedia Computer Science* 212, 464–473.
- Hansen, D., Maddix, D.C., Alizadeh, S., Gupta, G., Mahoney, M.W., 2023. Learning physical models that can respect conservation laws, in: *International Conference on Machine Learning*, PMLR. pp. 12469–12510.
- Hu, C., Cui, Y., Zhang, W., Qian, F., Wang, H., Wang, Q., Zhao, C., 2023. Solution of conservative-form transport equations with physics-informed neural network. *International Journal of Heat and Mass Transfer* 216, 124546.
- Hu, H., Qi, L., Chao, X., 2024. Physics-informed neural networks (pinn) for computational solid mechanics: Numerical frameworks and applications. *Thin-Walled Structures* , 112495.
- Jagtap, A.D., Kharazmi, E., Karniadakis, G.E., 2020. Conservative physics-informed neural networks on discrete domains for conservation laws: Applications to forward and inverse problems. *Computer Methods in Applied Mechanics and Engineering* 365, 113028.
- Jahani-Nasab, M., Bijarchi, M.A., 2024. Enhancing convergence speed with feature enforcing physics-informed neural networks using boundary conditions as prior knowledge. *Scientific Reports* 14, 23836.

- Jiang, Q., Shu, C., Zhu, L., Yang, L., Liu, Y., Zhang, Z., 2023. Applications of finite difference-based physics-informed neural networks to steady incompressible isothermal and thermal flows. *International Journal for Numerical Methods in Fluids* 95, 1565–1597.
- Kalita, J.C., Dalal, D., Dass, A.K., 2001. Fully compact higher-order computation of steady-state natural convection in a square cavity. *Physical Review E* 64, 066703.
- Kaplarević-Mališić, A., Andrijević, B., Bojović, F., Nikolić, S., Krstić, L., Stojanović, B., Ivanović, M., 2023. Identifying optimal architectures of physics-informed neural networks by evolutionary strategy. *Applied Soft Computing* 146, 110646.
- Karnakov, P., Litvinov, S., Koumoutsakos, P., 2024. Solving inverse problems in physics by optimizing a discrete loss: Fast and accurate learning without neural networks. *PNAS nexus* 3, pgae005.
- Karniadakis, G.E., Kevrekidis, I.G., Lu, L., Perdikaris, P., Wang, S., Yang, L., 2021. Physics-informed machine learning. *Nature Reviews Physics* 3, 422–440.
- Katende, R., Kasumba, H., Kakuba, G., Mango, J.M., 2024. Some results on neural network stability, consistency, and convergence: Insights into non-iid data, high-dimensional settings, and physics-informed neural networks. *arXiv preprint arXiv:2409.05030* .
- Kim, K., Baek, S.J., Sung, H.J., 2002. An implicit velocity decoupling procedure for the incompressible navier–stokes equations. *International journal for numerical methods in fluids* 38, 125–138.
- Ku, H.C., Hirsh, R.S., Taylor, T.D., 1987. A pseudospectral method for solution of the three-dimensional incompressible navier-stokes equations. *Journal of Computational Physics* 70, 439–462.
- LeCun, Y., Bengio, Y., Hinton, G., 2015. Deep learning. *nature* 521, 436–444.
- Lim, K.L., Dutta, R., Rotaru, M., 2022. Physics informed neural network using finite difference method, in: *2022 IEEE International Conference on Systems, Man, and Cybernetics (SMC)*, IEEE. pp. 1828–1833.
- Lin, S., Chen, Y., 2022. A two-stage physics-informed neural network method based on conserved quantities and applications in localized wave solutions. *Journal of Computational Physics* 457, 111053.

- Lou, Q., Meng, X., Karniadakis, G.E., 2021. Physics-informed neural networks for solving forward and inverse flow problems via the boltzmann-bgk formulation. *Journal of Computational Physics* 447, 110676.
- Malalasekera, W., 2007. *An introduction to computational fluid dynamics: the finite volume method*. Pearson Prentice Hall.
- McClenney, L.D., Braga-Neto, U.M., 2023. Self-adaptive physics-informed neural networks. *Journal of Computational Physics* 474, 111722.
- Mei, D., Zhou, K., Liu, C.H., 2024. Unified finite-volume physics informed neural networks to solve the heterogeneous partial differential equations. *Knowledge-Based Systems* 295, 111831.
- Meng, Y., Zhou, R., Mukherjee, A., Fitzsimmons, M., Song, C., Liu, J., 2024. Physics-informed neural network policy iteration: Algorithms, convergence, and verification. *arXiv preprint arXiv:2402.10119* .
- Meng, Z., Qian, Q., Xu, M., Yu, B., Yıldız, A.R., Mirjalili, S., 2023. Pinn-form: a new physics-informed neural network for reliability analysis with partial differential equation. *Computer Methods in Applied Mechanics and Engineering* 414, 116172.
- Moser, P., Fenz, W., Thumfart, S., Ganitzer, I., Giretzlehner, M., 2023. Modeling of 3d blood flows with physics-informed neural networks: comparison of network architectures. *Fluids* 8, 46.
- Moukalled, F., Mangani, L., Darwish, M., Moukalled, F., Mangani, L., Darwish, M., 2016. *The finite volume method*. Springer.
- Nosrati, H., Emami Niri, M., 2024. Manipulating the loss calculation to enhance the training process of physics-informed neural networks to solve the 1d wave equation. *Engineering with Computers* 40, 1741–1769.
- Patankar, S., 2018. *Numerical heat transfer and fluid flow*. CRC press.
- Raissi, M., Perdikaris, P., Karniadakis, G., 2019. Physics-informed neural networks: A deep learning framework for solving forward and inverse problems involving nonlinear partial differential equations. *Journal of Computational Physics* 378, 686–707.
- Rajvanshi, M.P., Ketcheson, D.I., 2024. Integral pinns for hyperbolic conservation laws, in: *ICLR 2024 Workshop on AI4DifferentialEquations In Science*.

- Rathore, P., Lei, W., Frangella, Z., Lu, L., Udell, M., 2024. Challenges in training pinns: A loss landscape perspective. arXiv preprint arXiv:2402.01868 .
- Sarabian, M., Babaei, H., Laksari, K., 2022. Physics-informed neural networks for brain hemodynamic predictions using medical imaging. *IEEE transactions on medical imaging* 41, 2285–2303.
- Shankar, P., Deshpande, M., 2000. Fluid mechanics in the driven cavity. *Annual review of fluid mechanics* 32, 93–136.
- Su, Z., Liu, Y., Pan, S., Li, Z., Shen, C., 2024. Finite volume physical informed neural network (fv-pinn) with reduced derivative order for incompressible flows. arXiv preprint arXiv:2411.17095 .
- Tao, W.Q., 2021. My 50-year life in studying heat transfer. *Applied Thermal Engineering* 194, 116947.
- Thomas, J.W., 2013. Numerical partial differential equations: finite difference methods. volume 22. Springer Science & Business Media.
- Wang, H., Qian, X., Sun, Y., Song, S., 2022a. A modified physics informed neural networks for solving the partial differential equation with conservation laws. Available at SSRN 4274376 .
- Wang, S., Bhartari, A.K., Li, B., Perdikaris, P., 2025. Gradient Alignment in Physics-informed Neural Networks: A Second-Order Optimization Perspective. arXiv e-prints arXiv:2502.00604.
- Wang, S., Li, B., Chen, Y., Perdikaris, P., 2024. Piratenets: Physics-informed deep learning with residual adaptive networks. *Journal of Machine Learning Research* 25, 1–51.
- Wang, S., Sankaran, S., Wang, H., Perdikaris, P., 2023a. An expert’s guide to training physics-informed neural networks. arXiv preprint arXiv:2308.08468 .
- Wang, S., Yu, X., Perdikaris, P., 2022b. When and why pinns fail to train: A neural tangent kernel perspective. *Journal of Computational Physics* 449, 110768.
- Wang, Y., Yang, S., 2024. Coupled integral pinn for conservation law. arXiv preprint arXiv:2411.11276 .
- Wang, Y., Zhong, L., 2024. Nas-pinn: neural architecture search-guided physics-informed neural network for solving pdes. *Journal of Computational Physics* 496, 112603.

- Wang, Z., Meng, X., Jiang, X., Xiang, H., Karniadakis, G.E., 2023b. Solution multiplicity and effects of data and eddy viscosity on navier-stokes solutions inferred by physics-informed neural networks. arXiv preprint arXiv:2309.06010 .
- Wei, C., Fan, Y., Zhou, Y., Liu, X., Li, C., Li, X., Wang, H., 2025. Physics-informed neural network based on control volumes for solving time-independent problems. *Physics of Fluids* 37.
- Wong, J.C., Chiu, P.H., Ooi, C., Dao, M.H., Ong, Y.S., 2023. Lsa-pinn: Linear boundary connectivity loss for solving pdes on complex geometry, in: 2023 International Joint Conference on Neural Networks (IJCNN), IEEE. pp. 1–10.
- Wu, G.Z., Fang, Y., Kudryashov, N.A., Wang, Y.Y., Dai, C.Q., 2022. Prediction of optical solitons using an improved physics-informed neural network method with the conservation law constraint. *Chaos, Solitons & Fractals* 159, 112143.
- Xiang, Z., Peng, W., Zhou, W., Yao, W., 2022. Hybrid finite difference with the physics-informed neural network for solving pde in complex geometries. arXiv preprint arXiv:2202.07926 .
- Xiao, Y., Yang, L., Du, Y., Song, Y., Shu, C., 2023. Radial basis function-differential quadrature-based physics-informed neural network for steady incompressible flows. *Physics of Fluids* 35.
- Xiao, Y., Yang, L., Shu, C., Dong, H., Du, Y., Song, Y., 2024. Least-square finite difference-based physics-informed neural network for steady incompressible flows. *Computers & Mathematics with Applications* 175, 33–48.
- Yuan, L., Ni, Y.Q., Deng, X.Y., Hao, S., 2022. A-pinn: Auxiliary physics informed neural networks for forward and inverse problems of nonlinear integro-differential equations. *Journal of Computational Physics* 462, 111260.
- Zhang, H., Xia, X., Wu, Z., Li, X., 2025. Physics-informed graph neural network based on the finite volume method for steady incompressible laminar convective heat transfer. *Physics of Fluids* 37.
- Zhu, T., Liu, D., Lu, Y., 2024. Finite-volume physics-informed u-net for flow field reconstruction with sparse data, in: International Design Engineering Technical Conferences and Computers and Information in Engineering Conference, American Society of Mechanical Engineers. p. V02AT02A021.
- Zoph, B., Le, Q.V., 2016. Neural architecture search with reinforcement learning. arXiv preprint arXiv:1611.01578 .